Cooperative ectodomain interaction among TCRαβ, CD3γε, and CD3δε enhances TCR mechanotransduction

Zhou Yuan[1-3†], Peiwen Cong[1,3†], Aswin Natarajan[4†], Chenghao Ge[1,3,a†], Stefano Travaglino[1,3], Saikiran Beesam[4], Danielle Grazette[4], Michelle Krogsgaard[4‡], Cheng Zhu[1-3‡]

[1]Wallace H. Coulter Department of Biomedical Engineering, [2]Georgia W. Woodruff School of Mechanical Engineering, [3]Petit Institute for Bioengineering and Bioscience, Georgia Institute of Technology, Atlanta, GA, USA; [4]Laura and Isaac Perlmutter Cancer Center and Department of Pathology, New York University Grossman School of Medicine, New York, NY, USA

[†]These authors contributed equally.

[‡]Contact: cheng.zhu@bme.gatech.edu, 1-404-894-3269 or Michelle.Krogsgaard@nyulangone.org, 212-263-9266,

[a]Present address: Amgen Inc., One Amgen Center Dr., Thousand Oaks, CA, USA

There are 200 words in abstract, 7077 words in main text (excluding abstract, methods, references and figure legends). The manuscript also includes 7 figures, 1 table and 70 references plus 5 supplementary figures, 2 supplementary tables, and 11 supplementary videos.

ABSTRACT

The T-cell receptor (TCR) complex comprises TCRαβ, CD3γε, CD3δε, and CD3ζζ. TCRαβ engagement with peptide-bound major histocompatibility complex (pMHC) triggers CD3 phosphorylation, which is regulated by mechanical force. However, the inner workings of the TCR mechanotransduction machinery remains unclear. TCR ectodomain (ECD) interactions have been inferred from structural and mutagenesis studies. Due to their extreme weakness, however, direct measurements of affinity had failed and of force regulation have never been attempted. Here we measured two-dimensional affinities and force-dependent lifetimes of interactions among TCRαβ, CD3γε, and CD3δε ECDs, showing a cooperative CD3δε–TCRαβ–CD3γε catch bond with longer-lasting lifetime that exceeds the TCR–pMHC bond lifetime. Molecular dynamics stimulations revealed a central interacting region surrounded by TCR ECDs and identified critical interacting residues at their interfaces. Interfering TCR ECD interactions by antibodies impaired TCR–pMHC interaction and T cell function. Mutating residues that mediate TCR ECD *cis*-interactions with CD3s altered the catch bond of TCR–pMHC *trans*-interaction, which correlates with changed T cell cytokine production. Thus, TCR mechanotransduction is supported by cooperative TCR ECD interactions, which regulates T cell function. Our results provide a missing link between pMHC ligation and CD3 signaling and may guide future TCR engineering design for immunotherapies.

44 **INTRODUCTION**

45 Antigen recognition by the TCR-CD3 complex (hereinafter denoted as TCR) initiates T cell
46 activation, leading to subsequent proliferation, effector function, and differentiation of T cells (*1*).
47 Despite extensive research, the key question of how TCR–pMHC binding induces T cell signaling
48 remains unclear. Proposed models for TCR triggering include conformational change,
49 mechanotransduction, and dynamically-driven allostery (*1-7*). Indeed, recent *in vitro* experiments
50 have demonstrated that T cells exert endogenous forces on the TCR via engaged pMHC (*8-10*)
51 and that mechanical force not only can induce conformational change and regulate the lifetime of
52 TCR–pMHC bonds (*11-15*) but can also trigger T cell signaling (*11, 16-18*). Also, nuclear
53 magnetic resonance (NMR) (*19, 20*) and molecular dynamics (MD) (*20, 21*) studies have
54 suggested that pMHC binding impacts the dynamics of TCR allosterically, providing another
55 possible mechanism for TCR triggering that is not mutually exclusive to the mechanosensor
56 mechanism (*3*). To sustain mechanical force exerted on, and/or transmit dynamics allosterically
57 through, its structure, the TCR must be held together by non-covalent interactions between the
58 ECDs, connecting peptide (CP), and transmembrane domains of its subunits. Extracellularly,
59 TCRαβ constant domains (Cα/Cβ) are proximal to both CD3γε and CD3δε ECDs (*22-26*)
60 (hereinafter we omit "ECD"), but are thought to only interact weakly due to the inability to detect
61 binding by three-dimensional (3D) measurement techniques such as the surface plasmon resonance
62 (SPR, Supplementary Fig. 1a). However, biochemical, mutagenesis, and solution NMR studies
63 have suggested CD3-binding sites on the TCRαβ the mutations on which impair TCR stability and
64 functionality (*22-24, 27*), indicating the relevance of these interactions. Suggested roles of these
65 weak ECD interactions include guiding the proper spatial arrangement of the TCR assembly,
66 stabilizing the complex structure, and amplifying the TCR signal transduction for T cell activation

67 (*22, 27*). Several structural studies tried to elucidate the molecular details of the TCRαβ–CD3
68 dynamic interactions in the absence of mechanical forces (*19, 20, 23, 24*), which is unlikely able
69 to resolve its mechanotransduction role of TCRαβ–CD3 interactions.

70 Using purified proteins and ultrasensitive mechanical techniques, the micropipette (*28, 29*)
71 and biomembrane force probe (BFP) (*11, 30*), we measured two-dimensional (2D) binding
72 affinities and force-dependent lifetimes of TCRαβ bonds with CD3γε, CD3δε, and both. Using
73 both force-free conventional MD (CMD) and steered MD (SMD) simulations based on the recently
74 published cryoEM structure (*26*), we analyzed TCRαβ–CD3 interactions in the absence and
75 presence of pulling forces, finding that perturbing the TCRαβ–CD3 interactions affects the TCR–
76 pMHC catch bond and T cell function. Mutagenesis experiment found that mutating residues at
77 the TCRαβ-CD3 interface to enhance interaction under force prolonged the TCR–pMHC lifetime
78 and T cell function. Our results demonstrated catch bond formation and cooperativity in these
79 interactions and delineated molecular details of a TCR triggering model.

80

81 **RESULTS**

82 **Antibody interfering TCRαβ–CD3 interactions impairs TCR–pMHC interaction and T cell**
83 **function**

84 To investigate how TCRαβ–CD3 interactions support the TCR antigen recognition and
85 mechanotransduction, we first asked whether interfering TCRαβ–CD3 *cis*-interactions affects
86 TCR–pMHC *trans*-interaction. Previous studies have identified two monoclonal antibodies
87 (mAbs), H57 (against TCRβ constant domain (*31*)) and 2C11 (against CD3ε (*32*)), whose binding
88 likely block TCRαβ–CD3 interactions (Fig. 1A). To confirm their blocking effects, we coated 2C
89 TCRαβ and mouse CD3γε ECD proteins on the respective surfaces of two human red blood cells

90 (RBCs) that were pressurized and opposingly aligned to measure 2D binding by the micropipette
91 adhesion frequency (MAF) assay (*28, 29*) (Fig. 1B, *upper*). As expected, adhesion frequencies
92 were significantly lower in the presence than absence of full-length H57 and 2C11, and of the
93 single-chain variable fragment (scFv) of H57, but not of the control mAb F23 (against TCRβ
94 variable domain (*33*)) (Fig. 1C).

95 To answer our question of the preceding paragraph, we again used the MAF assay to
96 measure binding between 2C TCR expressing cells and RBCs coated with SIYR:H2-K^b (Fig. 1B
97 *lower*). Remarkably, adhesion frequencies mediated by TCR–pMHC binding were significantly
98 lower in the presence than absence of H57 Fab and 2C11 Fab, but not of F23 Fab (Fig. 1D). This
99 is despite that neither mAb Fabs hinder the TCR–pMHC bonding interface (Fig. 1A), nor do they
100 affect the access of SIYR:H-$2K^b$ tetramer to 2C TCR on the cell surface (Fig. S1A). Interesting,
101 the adhesion frequency reduction by H57 scFv, a smaller fragment than Fab, was no longer
102 significant (Fig. 1D). To obtain further supporting evidence, we used the BFP (Fig. 1E) force-
103 clamp assay (*11-13, 15*) (Fig. 1F) to measure the effects of H57 on the force-dependent lifetimes
104 of 2C TCR–SIYR:H-$2K^b$ bonds at 10 pN clamp force. Consistent with the MAF assay results,
105 bond lifetimes were significantly shortened in the presence than absence of H57 Fab but not scFv
106 (Fig. 1G).

107 To determine the functional consequence, if any, of the reduced adhesion frequency and
108 bond lifetime of the TCR–pMHC *trans*-interaction by antibody interference of the TCRαβ–CD3
109 *cis*-interactions, we measured the IL-2 production of T cells in response to SIYR peptide
110 stimulation. Remarkably, the presence of the H57 Fab and 2C11 Fab greatly reduced the IL-2
111 production compared to Fab of control mAb F23 and of non-binding mAb H28 (Fig. 1H),

112 establishing the correlation of reduced TCR–pMHC binding and bond lifetime with reduced T cell
113 function.
114
115 **Low affinities, fast off-rates, and catch bonds of the TCRαβ–CD3 interactions**
116 We next sought to characterize the TCR ECD interactions. Like previous attempts (*34*), SPR was
117 unable to detect binding (Fig. S1B). We therefore measured 2D kinetics among hybrid 2B4 TCRαβ
118 (of mouse 2B4 TCRαβ variable domains fused with human LC13 TCRαβ constant domains) (*24,*
119 *35*), human CD3δε, and human CD3γε using the MAF assay with the same setup and coating
120 strategy as Fig. 1B (*top*). The anticipated low affinity binding was overcome by the ultra-
121 sensitivity of the MAF assay, which allowed us to measure specific adhesion frequencies (Fig.
122 S1C) from which the effective 2D affinities of TCRαβ–CD3γε, TCRαβ–CD3δε and CD3γε–
123 CD3δε heterotypic interactions were evaluated (Fig. 2A, Fig. S1D,J). To accurately analyze the
124 fast TCRαβ–CD3 dissociations, we used the BFP (Fig. 1E) thermal fluctuation assay (Fig. 2B) (*29,*
125 *36*) to measure off-rates of bonds between molecules coated on opposing glass beads (Fig. 2C, Fig.
126 S1J). We calculated the effective 2D on-rates by multiplying affinities with off-rates (Fig. 2D, Fig.
127 S1J). These TCRαβ–CD3 interactions are indeed of very low affinities (2-4 × 10^{-6} μm^4) and rapid
128 zero-force off-rates (>10 s^{-1}), attesting to the ultrasensitivity of our mechanical assays (*37, 38*).
129 We (*11-13*) and others (*14, 15*) have shown that mechanical force modulates TCR–pMHC
130 interactions and amplify antigen discrimination (*11, 12, 14*). Force may modulate TCRαβ–CD3
131 interactions in a similar fashion. This hypothesis is based on the observation that upon pMHC
132 ligation, the binding-induced NMR signal perturbation propagates to the Cβ site involved in the
133 putative CD3 interactions (*20*), suggesting an allosteric pathway even in the absence of force. In
134 the presence of force, this pathway may allow force-encoded information to transmit from pMHC

135 to CD3 through TCRαβ, thereby triggering signaling. To test our hypothesis, we used BFP force-
136 clamp assay (Fig. 1E,F) to measure the lifetimes of single-bonds of specific (Fig. S1E-G) TCRαβ–
137 CD3γε, TCRαβ–CD3δε, and CD3γε–CD3δε interactions under a range of constant forces (Fig.
138 2E). We found that all three interactions formed catch bonds where their lifetimes were prolonged
139 by forces below ~10-20 pN until higher forces overpowered the bonds to shorten their lifetimes
140 (*i.e.*, slip bonds). Our data show that these interactions can bear force, supporting our hypothesis
141 that information of antigen recognition can be transmitted mechanically through TCRαβ–CD3
142 interactions.

143 For comparison, we also measured 2D binding parameters of the specific (Fig. S1I)
144 interaction between fully assembled 2B4 TCR on the cell surface with K5:I-E^k (Fig. 2A,C,D,F).
145 This TCR–pMHC interaction has a comparable affinity to TCRαβ–CD3 interactions but much
146 longer bond lifetimes over the entire range of forces (Fig. 2F), seemingly suggesting that the
147 TCRαβ–CD3 *cis*-interactions may be less stable than the TCR–pMHC *trans*-interaction, therefore
148 challenging our mechanical transmission hypothesis. Our CD3δε–CD3γε interaction data (Fig.
149 2A,C,D,E) are consistent with the TCR structure showing contact between CD3γε and CD3δε (*26*).
150 The 1:1:1 stoichiometry among TCRαβ and the two CD3 heterodimers raised a question of whether
151 TCRαβ binds CD3γε and CD3δε concurrently to form trimolecular bonds; if so, whether this
152 concurrent binding is independent or cooperative; and if cooperative, how much enhanced stability
153 the cooperative binding results and whether the enhancement meets the aforementioned challenge.
154

155 **CD3γε and CD3δε bind TCRαβ cooperatively to enhance TCR stability**

156 To address the above questions, we used the MAF assay to compare the specific (Fig. S1C) 2D
157 binding of TCRαβ-bearing RBCs to RBCs coated with either CD3γε, CD3δε or both at a 1:1 ratio

158 ("CD3m"). The average number of TCRαβ bonds with indicated CD3 species, $<n>_\gamma$, $<n>_\delta$, and
159 $<n>_m$, were calculated from the adhesion frequencies P_a, and normalized by the densities of TCRαβ
160 ($m_{\alpha\beta}$) and CD3ε (m_ε) to remove the influence of uneven protein coating (Fig. 3B). For TCRαβ
161 binding to either CD3 species, the normalized bond numbers ($<n>_\gamma/m_{\alpha\beta}m_{\gamma\varepsilon}$ and $<n>_\delta/m_{\alpha\beta}m_{\delta\varepsilon}$) at
162 steady-state are identical to their effective 2D affinities ($A_cK_{a,\gamma}$ and $A_cK_{a,\delta}$) shown in Fig. 2A
163 because m_ε equals $m_{\gamma\varepsilon}$, $m_{\delta\varepsilon}$, or $m_{\gamma\varepsilon} + m_{\delta\varepsilon}$ depending on whether the RBCs were coated with CD3γε,
164 CD3δε, or both. For TCRαβ binding to both CD3s, $<n>_m/m_{\alpha\beta}m_\varepsilon$ would be equal to the average of
165 the effective 2D affinities of the two bimolecular interactions $(A_cK_{a,\gamma} + A_cK_{a,\delta})/2$, should CD3γε
166 and CD3δε bind TCRαβ independently rather than cooperatively. In the presence of cooperative
167 binding, on the other hand, the whole $<n>_m$ represents total bonds that include not only two
168 bimolecular bond species, $<n>_\gamma$ and $<n>_\delta$, but also a trimolecular bond species, $<n>_{\delta\gamma}$, as denoted
169 by their respective subscripts. In such a case, the normalized bond number resembles avidity
170 because of the simultaneous binding of CD3γε and CD3δε to the same TCRαβ. The presence of
171 the trimolecular bonds was detected by the significantly higher $<n>_m/m_{\alpha\beta}m_\varepsilon$ value than the value
172 of $<n>_\gamma/m_{\alpha\beta}m_{\gamma\varepsilon}$, $<n>_\delta/m_{\alpha\beta}m_{\delta\varepsilon}$, or their average $[(<n>_\gamma/m_{\alpha\beta}m_{\gamma\varepsilon} + <n>_\delta/m_{\alpha\beta}m_{\delta\varepsilon})/2]$ (Fig. 3C),
173 indicating cooperativity. To quantify the enhancement resulted from cooperativity, we calculated
174 the relative change in average bond numbers of the whole ($<n>_m$) over the sum of the parts $[(<n>_\gamma$
175 $+ <n>_\delta)]$, finding a ~47% increase in bond numbers (Fig. 3D), indicating that the trimolecular
176 bonds comprise no less than 32% of the total bonds.

177 Based on our previous observations in other systems (*39, 40*), we hypothesized that the
178 trimolecular bond of TCRαβ with both CD3γε and CD3δε would be more stable, hence could
179 sustain force for a longer time, than either TCRαβ–CD3γε or TCRαβ–CD3δε bimolecular bond.
180 To test this hypothesis, we used the BFP force-clamp assay (*11*) (Fig. 1E,F) to measure the specific

181 (Fig. S1E,H) force-dependent lifetimes of TCRαβ-bearing glass beads bonding with BFP beads
182 concurrently coated with CD3γε and CD3δε at a 1:1 molar ratio (Fig. 3A). The average bond
183 lifetimes ($<t>_m$, red circle in Fig. 3E) peak at 13 pN with a value of 1.5 s and are significantly
184 longer than the averaged lifetimes of TCRαβ bond with either CD3 ($<t>_\gamma$ or $<t>_\delta$, peaked at ~10 or
185 ~20 pN, with a value of ~0.6 s for both) at all forces tested (blue triangle and orange square in Fig.
186 3E, replotted from Fig. 2E). The $<t>_m$ *vs*. force plot exhibits a catch bond more pronounced than
187 the TCRαβ–CD3γε and TCRαβ–CD3δε catch bonds, but matches the 2B4 TCR–K5:I-E^k catch
188 bond (Fig. 2F, lifetime peaked at 15 pN with a value of 1.6 s). We reason that the longer $<t>_m$
189 could not have been caused by the low-probability multi-bond binding events in the TCRαβ–
190 CD3γε and/or TCRαβ–CD3δε interactions that would have occurred more frequently under the
191 mix coating than the single coating conditions. This is because the adhesion frequencies in all
192 conditions were kept low (≤20%) by adjusting the site densities of the molecules coated on the
193 beads, predicting ≥89% of single-bonds among all binding events (*28*). Instead, our results indicate
194 the presence of a new species, the CD3δε–TCRαβ–CD3γε trimolecular bonds, whose average
195 lifetime $<t>_{\delta\gamma}$ augmented the value of $<t>_m$, indicating cooperativity. To further quantify the
196 enhancement of cooperative on interaction lifetime, we calculated the relative change of the whole
197 (*i.e.*, $<t>_m$) over the average of the parts (*i.e.*, $<t>_\delta$ and $<t>_\gamma$) weighted by their respective
198 likelihoods of bond formation, finding a ~63-424% increase in averaged bond lifetime over the
199 force range of 0-22 pN (Fig. 3F).

200 The cooperativity analyses in terms of bond lifetime and bond number are similar in
201 principle but different on basis. Assuming independent interactions, multi-species receptor–ligand
202 bonds as a whole have been shown to be the sum of component single-species bonds (*41-43*). Our
203 data do not follow this additive prediction (Fig. 3D), invalidating the assumption of independent

204 binding, therefore signifying cooperativity. Similarly, the average bond lifetime can be calculated
205 either from all measurements as a whole or from subpopulation averages as parts, provided that
206 the whole contains the assumed parts at the assumed proportions. Our data do not follow this
207 commutative prediction (Fig. 3F), invalidating the assumptions regarding the subpopulation
208 identities, their proportions, or both, therefore signifying cooperativity. Thus, our data demonstrate
209 that cooperative binding enhances bond formation among TCRαβ, CD3γε, and CD3δε comparing
210 to individual TCRαβ–CD3γε or TCRαβ–CD3δε bond formation alone; this cooperativity further
211 stabilizes the ECD interaction of the TCR subunits under force.

212 To identify the trimolecular bond contribution to average bond lifetimes, we compared
213 survival probabilities of individual TCRαβ bonds with single CD3 species (γ and δ) and with
214 CD3m (m) in four force bins (Fig. 3G), which are multi-exponentially distributed (except for the
215 two bimolecular interactions at zero-force), suggesting the presence of multiple bound states,
216 multiple bond species, or both. We modeled the dissociation from the weak and strong states using
217 respective fast (-f) and (-s) off-rates, and the transitions between the two states by activation (a)
218 and deactivation (-a) rates (*44*), all of which depend on force according to the Bell equation (*45*)
219 (Fig. S2A). Each kinetic rate $k_{\mathrm{i,j}}$ (i = -f, -s, a, and -a; j = γ, δ, and m) has two Bell parameters: the
220 zero-force rate $k^0_{\mathrm{i,j}}$ and the width of the energy well $x_{\mathrm{i,j}}$ that kinetically traps the bond. The zero-
221 force fast dissociation rates $k^0_{-\mathrm{f,j}}$ for the bimolecular complexes were measured by the thermal
222 fluctuation experiments (Fig. 3G, *left*). By fitting the kinetic model to the force-lifetime
223 distributions as a whole (Fig. S2B-D), the remaining rates were evaluated as depicted in Fig. S2E-
224 G. The fractions of the strong state, expressed as $1/(1 + k_{\mathrm{-a,j}}/k_{\mathrm{a,j}})$, are plotted *vs.* force in Fig. S2H,
225 indicating that force rapidly shifts the bonds from the weak to strong state. This global fitting
226 predicts three mean ± SD lifetime *vs.* force curves for both bimolecular bonds as well as the mixed

227 bonds that agree well with measurements (Fig. 3E). It also generates a set of best-fit parameters
228 (Fig. S2I) that inform the detailed kinetic process. The TCRαβ–CD3γε and TCRαβ–CD3δε bonds
229 dissociate similarly, with comparable fast rates from the weak state (11.1 s^{-1} and 11.4 s^{-1} by
230 measurement) and similar slow rates from the strong state (0.196 s^{-1} and 0.184 s^{-1} by fitting). The
231 CD3δε–TCRαβ–CD3γε bond dissociates at 0.700 s^{-1} from the weak state, a 16-fold reduction, and
232 0.0519 s^{-1} from the strong state, a 4-fold reduction, respectively, compared to the bimolecular bond
233 dissociations. Using the kinetic model and the best-fit parameters, we calculated the cooperativity
234 index *vs*. force curve, which compares well with direct measurements (Fig. 3F). We plotted the
235 fraction of trimolecular bonds *vs.* lifetime at three different forces in Fig. 2h, showing that as the
236 force increased, the trimolecular bond became dominant to contribute mainly to the long lifetimes.
237 These results show that the force-enriched long-lived CD3δε–TCRαβ–CD3γε bonds are the kinetic
238 underpinning for the mechanical-reinforced cooperativity.
239
240 **MD simulated TCR ECD binding free energies and bond lifetimes verify cooperativity**
241 To corroborate the experimentally observed cooperative binding, we performed force-free CMD
242 simulations (*46*) on the TCRαβ–CD3γε (Video S1), TCRαβ–CD3δε (Video S2), CD3γε–CD3δε
243 (Video S3), and CD3δε–TCRαβ–CD3γε (Video S4) complexes modified from the cryoEM
244 structure (*26*) (Fig. 4A, Fig. S3A). All equilibrated ECDs remained bounded throughout 200 ns
245 simulation, but the contact areas (Fig. S3B) and binding free energy (Fig. S3C) of the standalone
246 dimeric structures varied slightly compared to the corresponding pairwise interfaces as part of the
247 trimeric structure (Fig. 4B,C, *left* and *middle* groups) due to the accommodation of TCRαβ or a
248 second CD3. The dimeric interfaces of TCRαβ with CD3γε and CD3δε were adjacent with little
249 overlap, so their combined contact area in the trimeric complex was only slightly smaller than the

250 sum of their contact areas in the dimeric complexes (Fig. 4B, *right* group). However, this loss of
251 contact area from limited steric interference was more than made up by the gain in the total contact
252 area when the contact area between CD3γε and CD3δε in the trimeric complex was included.
253 Indeed, the formation of a trimeric structure substantially lowered the total binding free energy
254 when the contribution from the CD3γε–CD3δε interaction was included (but not when it is
255 excluded) (Fig. 4C, *right* group). Since affinity is proportional to the exponential of binding free
256 energy (in the unit of $k_B T$), our CMD simulations provide independent evidence and molecular
257 foundation for the experimental observations of increased binding likelihood due to the
258 cooperative binding of TCRαβ simultaneously to CD3γε and CD3δε (Fig. 3D).

259 To compute the prolongation of the bond lifetime due to the cooperativity of the
260 trimolecular assembly, we applied SMD (*47*) to simulate dissociation of the dimeric and trimeric
261 complexes by force. We used both force-clamp and force-ramp SMD to pull on the TCRαβ N-
262 terminus with the C-terminus of CD3γε or CD3δε, or the C-termini of the CD3γε–CD3δε complex
263 anchored as fixed points (Fig. S3D). We utilized 100-200 pN clamping forces to accelerate their
264 dissociations within achievable simulation timescales. The minimum distances and pulling
265 distances between the TCRαβ and CD3γε, CD3δε, or both were solved by monitoring the
266 simulated complex dynamic under a constant force (Fig. S3E,F). A sudden increase in the
267 minimum distance signified dissociation from which the bond lifetime was measured (Fig. 4D,
268 Fig. S3E, Video S5-7). The simulated force-dependent lifetimes of bimolecular and trimolecular
269 bonds were summarized in Fig. 4E. The TCRαβ–CD3γε bond dissociated slower than the TCRαβ–
270 CD3δε bond at all forces, consistent with its larger contact area and lower binding free energy
271 (Fig. 4B,C). Both had relatively short lifetimes that decreased with increasing force following the
272 Bell equation (*45*), in agreement with their slip bond behavior under such high loads (Fig. 3E). By

273 contrast, the trimolecular bonds survived at least an order of magnitude longer than the
274 corresponding dimer lifetimes, falling apart at 626, 404, and 233 ns under 150, 175, and 200 pN,
275 respectively. Their lifetimes also significantly exceeded the predicted non-cooperative values
276 calculated from their respective TCRαβ–CD3γε and TCRαβ–CD3δε dissociation time,
277 manifesting strong cooperativity under external force (Fig. 4F).

278 We also simulated force-ramp unbinding to measure the rupture forces of the partial and
279 full TCR ECD complexes (Fig. S3G). The larger rupture forces of the CD3δε–TCRαβ–CD3γε
280 complex than those of the TCRαβ–CD3γε and TCRαβ–CD3δε complexes under the same loading
281 rate further confirms the sturdier binding for the trimolecular complex. Together, our MD
282 simulations suggest that cooperativity enhances the interactions among ECDs of the TCR complex
283 by forming a stronger CD3δε–TCRαβ–CD3γε trimolecular bond, particularly when pulled, as
284 measured by contact area, binding free energy, bond lifetime, and rupture force.

285

286 **Occupancy analysis reveals TCR-CD3 contacts responsible for force-enhanced cooperativity**

287 To elucidate the mechano-responsiveness and cooperativity of TCRαβ-CD3 interactions, we
288 surveyed the contact residues between TCRαβ and CD3γε, CD3δε (hereinafter referred as
289 CD3δε'), or both found in MD simulations using residue-to-residue (RR) occupancy index (OI).
290 The degree of contact between two residues was quantified by the cumulative fraction of time
291 during which their distance is below 4 Å. We determined two RR-OI matrices of pairwise contacts
292 of individual TCRαβ residues with CD3γε and CD3δε' residues from trimeric CMD (Fig. S4A)
293 and SMD (Fig. S4B), respectively. The residue-by-residue sums of the two RR-OI matrices, ΣRR-
294 OI, was displayed in Fig. 5A (Table S1A), to highlight residues that made contact in both the
295 absence and presence of forces. These RR-OI matrices contain high-content information derived

296 from analysis of dynamic structures in the absence and presence of the force not obtainable from
297 the static image: the numbers of contact residues (RR-OI>0) revealed by CMD and SMD are,
298 respectively ~10% and ~14% more than that observed from the cryoEM structure.

299 The residue-by-residue differences of the two RR-OI matrices, ΔRR-OI, was shown in Fig.
300 5B (and Fig. S4C, Table S1B), to distinguish the force-stabilized and -destabilized residue pairs
301 with increased (red) or decreased (blue) OI values respectively upon applying forces. The contact
302 regions include force-stabilized residue pairs between the Cα DE loop and CD3δ AB and DE loops
303 and between the Cβ Helix 4 and CD3δ AB loop. The contact regions also include force-
304 destabilized residue pairs between the Cα AB loop and CD3ε FG loop, between the Cβ CC' loop
305 and CD3δ AB loop, and between the Cβ CC' loop and CD3ε' FG loop. Regions with more force-
306 stabilized than force-destabilized contact residue pairs were seen between the Cβ Helix 4 and
307 CD3δ EF loop, between the Cβ Helix 4-F strand and CD3γ AB loop, and between the Cβ G-strand
308 and CD3ε CD and FG loops, and Helix 2.

309 To analyze the force-enhanced cooperativity, we overlaid the 1D residue-to-domain (RD)-
310 OI profiles of the contact residues from the SMD simulation of the TCRαβ–CD3γε (blue), TCRαβ–
311 CD3δε' (orange), and CD3δε'–TCRαβ–CD3γε (red) complexes (Fig. 5C, Table S1C), quantifying
312 the individual residues of TCR α and β chains contacting all CD3 residues, as well as CD3 γ, ε, ε'
313 and δ chains contacting all TCRαβ residues. As shown, the cooperative TCR-CD3 interaction is
314 mediated by secondary structures in TCRαβ, CD3γε, and CD3δε' identified in Fig. 5A-B. The
315 regions forming the TCRαβ–CD3γε and TCRαβ–CD3δε' interfaces are the same regardless of
316 whether they are in the bimolecular or trimolecular complexes, showing minimal interference
317 between CD3γε and CD3δε' when they bind TCRαβ concurrently. This remains true when
318 observed using CMD (Fig. S4D), agree with the result from Fig. 5B-C. Further, the RD-OI values

319 of some secondary structures, including CD3δ AB, DE, and EF loops, Cα DE loop, and Cβ Helix
320 4, were higher in the trimeric than the dimeric complexes under force (Fig. 5C), but show much
321 less differences without force (Fig. S4D). These comparisons identify regions contributing to the
322 force-enhanced cooperative contacts (Fig. S4E).

323 To further quantify the contact level between two domains, we averaged positive RD-OI
324 across all contacting residues from a particular chain to obtain domain-to-domain (DD) OI,
325 providing a global view of the TCR-CD3 inter-subunit interactions. We plotted the force-free DD-
326 OI *vs.* their force-clamp counterpart in Fig. 5D for CD3γ, ε, ε' or δ contacting TCRαβ (*top*), and
327 TCRα or β contacting CD3γε, δε' or both (*bottom*). Since the *x*- and *y*-coordinates represent the
328 DD-OI values calculated from the SMD and CMD, respectively, a point above and below the 45°
329 diagonal line reflects force-reduced and force-enhanced interaction, respectively. The dashed line
330 connecting two points of the same CD3 or TCR chains (marked by the same symbol) tracks the
331 different DD-OI values calculated from the dimeric (TCRαβ contacting CD3γε or CD3δε',
332 indicated by γε or δε') and trimeric (CD3δε'–TCRαβ–CD3γε, indicated by tri) complexes.
333 Compared to a point near the origin, the one further away from the origin contributes more to the
334 inter-subunit contact because it has larger DD-OI value(s) under force-free and/or force-clamp
335 conditions. For example, in the TCRαβ–CD3δε' dimeric complex, the δ chain contacted TCRαβ
336 with a force-clamp DD-OI of 0.19 and a force-free DD-OI of 0.37, showing an overall force-
337 reduced contact; however, in the CD3δε'–TCRαβ–CD3γε trimeric complex, the δ chain contacted
338 TCRαβ with a force-clamp DD-OI of 0.46 and a force-free DD-OI of 0.39, showing an overall
339 force-enhanced contact (Fig. 5D, *top, closed square*). Generally, we found that points labeled as
340 trimers were further away from the origin than their counterpart points labeled as dimers in all
341 dash-line-connected pairs except for the ε chain of CD3γε, explaining the cooperativity of the

342 trimeric complex. Further, all points labeled as trimers were below the diagonal line except for the
343 ε' chain of CD3δε', indicating the force enhancement of the CD3δε'–TCRαβ–CD3γε cooperative
344 interaction.

345 We also performed a parallel analysis that tracks the number of hydrogen bonds in
346 interfaces over simulation time, revealing that more hydrogen bonds were present in the trimeric
347 complex than the sum of parts in dimeric complex (Fig. S4F), agreeing with the conclusion of the
348 occupancy analysis.

349

350 **Structural basis of force-enhanced TCR-CD3 cooperativity**

351 To depict the spatial relationships of the contact residues, we mapped them onto the TCR
352 ECD quaternary structures by highlighting residues with high RD-OI levels. We first used
353 representative snapshots from 175-pN force-clamp SMD of the respective trimeric and two
354 dimeric complexes to show the CD3δε'–TCRαβ–CD3γε (Fig. 6A-C), TCRαβ–CD3γε (Fig. 6D,E),
355 and TCRαβ–CD3δε' (Fig. 6F) contact interfaces. We identified more contact residues in the same
356 spots of the trimeric complex (Fig. 6A-C) than dimeric complexes (Fig. 5D-F), and at the interfaces
357 of TCRαβ–CD3γε (Fig. 6D,E) than TCRαβ–CD3δε' (Fig. 6F) complex (Videos S8-10). These
358 observations provide the structural basis for the observed bond lifetime rank-order (Fig. 4E).
359 Examining these close-up views reveal a crowded pocket of interlocked contact residues at the
360 center of the CD3δε'–TCRαβ–CD3γε interface (Fig. 6A), which is built upon one of TCRαβ–
361 CD3γε interfaces (Fig. 6D) by recruiting additional residues nearby and even δ chain residues that
362 would be absent in the TCRαβ–CD3γε dimeric complex. Many high RD-OI residues near the core
363 of this patch have ring-containing sidechains, such as Y34γ, Y36γ, W259β, H226β, and F219β,

364 with sparse hydrogen bonds at peripheral. This suggests the hydrophobic nature of this core, where
365 π-π stackings significantly contribute to the patch stability.

366 To put into context of the above three subunit interfaces, we mark these spatial-proximal
367 contact residues on the zoom-out view of the full TCR-CD3 ECD (Fig. 6G, Video S11),
368 highlighting residues with >1.5 ΣRD-OI (sum of two RD-OI profiles from CMD and SMD). The
369 high ΣRD-OI residues in the center of this top-down view crosslink TCRαβ, CD3γε, and CD3δε'
370 (*blank circle*, Fig. 6G), with the contact residues residing on the two sides of the center patch to
371 bridge the TCRαβ with CD3γε on the left (*blue circle*) and δ chain of CD3δε' on the right (*orange*
372 *circle*). In addition, a contact residue patch at the CD3γε and CD3δε' interface is located right
373 below the center packet (*dotted black circle*). These observations suggest that to dissociate the
374 fully assembled TCR-CD3 complex may require disrupting at least three out of the four patches
375 that strong support the stability of the complex, revealing the structural basis of the trimolecular
376 cooperativity.

377 The residues with significant force-induced ΔRD-OI (difference of two RD-OI profiles
378 from SMD and CMD) concentrate at the three patches of the TCR-CD3 interfaces where red
379 indicates force-stabilizing (ΔRD-OI>0) and blue signifies force-destabilizing (ΔRD-OI<0)
380 contacts (Fig. 6H, Video S11). The RD-OI values of these contact residues at the core of the center
381 pocket calculated from SMD and CMD are both nearly 100%, making their difference nearly zero,
382 as reflected by their fade color. Interestingly, the force-stabilizing residues mark an outer red-color
383 ring around the center pocket, suggesting its expansion upon force application. The patch on the
384 right at the TCRαβ–CD3δε' interface comprises mostly force-stabilizing contact residues (*red*, Fig.
385 6H). By contrast, the patch on the left at the TCRαβ–CD3γε interface is mostly made up of force-

386 destabilizing contact residues (*blue*, Fig. 6H). This indicates that force tilts the TCRαβ clockwise
387 away from the CD3γε and toward the CD3δε'.

388 Parallel to the occupancy analysis, we defined the root-mean-square fluctuation (RMSF)
389 profiles to measure the flexibilities of individual residues inside the TCR-CD3 assembly, which
390 reflects its mechano-responsiveness from a different angle. To visualize the shifts in structural
391 flexibility, we projected the ΔRMSF values (difference between the SMD and CMD RMSF
392 profiles) on the TCR-CD3 ECD quaternary structure, with the thickness of the protein backbone
393 to represent residues' absolute RMSF in the presence of force (Fig. 6I, Video S11). Except for
394 TCRα, which experienced force-suppressed structural dynamics (*blue*, Fig. 6I), all other TCR-
395 CD3 chains fluctuated more under force (*red*, Fig. 6I), especially the ε' chain where the most
396 pronounced enhancement was observed. Here, the CD3δε' subunit waved around a hinge of the
397 tightened patch of TCRβ Helix 4 and CDδ AB loop, presenting distinctive force-induced motions
398 not observed in CD3γε.

399 Overall, only does the complete CD3δε'–TCRαβ–CD3γε assembly allow the formation of
400 a center patch of concentrated contact residues that are further shielded by surrounding patches,
401 explaining mechanistically the observed significantly prolonged lifetime of the trimeric complex.
402 External force enlarges and strengthens the center pocket, enhancing the cooperative CD3δε'–
403 TCRαβ–CD3γε binding. Furthermore, a spatial anti-correlation was observed between the force-
404 induced strengthening of inter-subunit contacts and force-enhanced structural dynamics, where
405 tighter contact leads to structural rigidification, and *vice versa*. Thus, differential mechano-
406 activation of TCRαβ-CD3 causes asymmetric mechano-responses of CD3δε' and CD3γε.

407

408 **Functional relevance of high occupancy interface residues**

409 To assess the functional significance of the structural information presented in Figs. 5-6,
410 we examined the contact residues on TCRαβ-CD3 interface indicated by the high RD-OI in force-
411 clamp SMD of the trimolecular complex, along with their functional effects described in the
412 literature (Table 1). Many of the identified contact residues were supported by literature (*23, 24,*
413 *26*), but our occupancy analysis provides new information on their binding partners and interaction
414 strength. For example, the contacts of Cα DE loop residues R185α with L29δ, S186α with L29δ,
415 E30δ, R32δ (Fig. S4B) were backed up by the literature evidence of R185α and S186α contacting
416 CD3δ (*26*). R185E and S186R substitutions impaired TCR assembly at the cell surface (*32*); R185
417 mutation abolished calcium spikes in T cells and reduced CD69 upregulation and ERK
418 phosphorylation in response to stimulations (*27*). Cβ helix 4 residues S216β, T218β, and F219β
419 interact with CD3δ AB loop E30δ, D31δ, R32δ and EF loop K62δ, I64δ (*23, 24*), among which
420 E30δ and D31δ form hydrophobic contacts with F219β (*26*). Mutations on Cβ T218R and F219R
421 and on their CD3δ interacting residues suppressed TCR surface expression by 70-80% (*32*). The
422 contact residues Y36γ, Cβ helix 4-F strand R224 (*23, 24*), N225 (*23, 24*), and H226 (*26*) have also
423 been identified as binding CD3, corresponding to previous finding that the R224E and H226E
424 mutations suppress TCRβ surface expression (*32*) and the N225A/H226A double mutations
425 sharply suppress IL-2 secretion upon T cell activation (*24*). Other contact residues identified by
426 our occupancy analysis include CD3ε H strand residue R115 and CD3γ AB loop residues D35,
427 Q37, E38 and G40 (Fig. S4B); their mutation resulted in poor surface expression of the CD3ε and
428 CD3γ, respectively (*32*). Our occupancy analysis agrees with the previous reports that the Cβ G
429 strand residue W259 interacts with the CD3γ AB loop as well as the CD3ε FG loop and H strand
430 through van der Waals contacts (*26*). Correspondingly, the W259R mutation boosts TCRβ surface
431 expression (*32*), and W259A mutation increases IL-2 production (*48*). Mutating its contact partner

432 CD3ε R115 impairs T cell activation by preventing the ligand binding-induced conformational
433 change to the cytoplasmic tail (*49*).

434 Further, we found literature supporting the functional relevance of our newly identified
435 TCRαβ–CD3 ECD contact residues. The Cα AB loop, whose residue K148α was identified by us
436 to contact N74ε and E91ε, was suggested to undergo conformational changes upon ligand binding,
437 leading to TCR triggering (*20, 50*). K148E substitution prevented stable formation of the TCR-
438 CD3 complex at the cell surface (*32*). The Cα DE loop residue M187α connects with R32δ; M187α
439 mutation impairs the T cell calcium signaling (*27*) and suppresses TCRα surface expression (*32*).

440 Intriguingly, we identified several TCRαβ residues with force-stabilizing contacts with
441 CD3s, indicated by increased ΔRD-OI values (Fig. 5B, Fig. S4C). The Cβ Helix 4 S216β and
442 T218β increased RD-OI from <0.5 by CMD to >0.8 by SMD, with a concurrent occupancy
443 increase in K62δ, suggesting the occurrence of force-strengthening of weak interactions, force-
444 induced forming of new interaction, or both, of S216 and/or T218 with CD3δ AB loop E30δ, D31δ
445 and R32δ as well as EF loop K62δ and I64δ. The Cβ helix 4-F strand residue P223β showed a 0.42
446 ΔRD-OI; correspondingly, the N222A/P223A mutation enhances IL-2 production upon cell
447 activation, suggesting a role for P223 in TCR signaling (*24*). Noticeably, N62ε displayed a 0.34
448 ΔRD-OI to contacts including Cβ G strand E257β, and G40γ exhibited a 0.42 ΔRD-OI to contact
449 Cβ Helix 4-F strand R224β. The Cβ G strand residue S255β showed a 0.30 ΔRD-OI, interacts with
450 high occupancy residue D63ε. Functionally, S255R mutation improves TCRβ surface expression
451 (*32*), and S255A mutation increases IL-2 production (*48*). These findings highlight possible roles
452 of force-induced strengthening/forming TCRαβ interactions with CD3 ECDs in T cell activation
453 (*4, 51*).

454 **Force-stabilizing TCRαβ–CD3 contact residues support prolonged TCR–pMHC bond**
455 **lifetime and enhanced T cell function**

456 We selected two pairs of the conserved residues, G182/K183 in the Cβ CC' loop and
457 N222/P223 in Cβ Helix 4-F strand (Fig. 7A,B) for further studies. K183 is a force-destabilizing
458 residue (ΔRD-OI = -0.22) mainly contracting with force-destabilizing residues L90 in the FG loop
459 and R115 in the CP region of CD3ε', whereas P223 is a force-stabilizing residue (ΔRD-OI = 0.42)
460 mainly contracting with force-stabilizing residue L90 in the FG loop of CD3ε (Table S2). By
461 comparison, their neighboring residues G182 and N222 show unchanged occupancies in the
462 presence and absence of force (ΔRD-OI = 0). G182 and P223 are newly identified and have
463 reported functional effects (Table 1). To investigate whether and how the contact residues in
464 TCRαβ–CD3 interface identified earlier support TCR mechanotransduction, we made double
465 alanine substitutions G182A/K183A (GK) and N222A/P223A (NP) in the 2B4 TCR to interfere
466 the TCRαβ–CD3 *cis*-interactions on hybridoma cell surfaces instead of using mAbs. To evaluate
467 their impact, we compared their *trans*-interactions with K5:I-E^k to the wild-type (WT) 2B4 TCR–
468 K5:I-E^k *trans*-interaction. The 2D affinity measured by MAF showed no difference among the WT
469 and mutant TCRs (Fig. 7C), indicating that mutations in TCR Cβ CC' loop and Helix 4-F strand
470 do not remotely affect binding of TCRαβ variable domain to pMHC at in the absence force. In the
471 presence of force, however, both double mutations altered TCR–pMHC bond lifetimes (Fig. 7D).
472 Comparing to the WT TCR, the NP mutation of a force-stabilizing residue at the TCRαβ–CD3ε
473 interface prolonged the peak lifetime of the TCR–pMHC interaction; by comparison, the GK
474 mutation of a force-destabilizing residue at the TCRαβ–CD3ε' interface shortened the peak
475 lifetime of the TCR–pMHC interaction (Fig. 7D,E). Importantly, the mutation-induced changes in

476 the peak bond lifetime correlated with the changes in IL-2 production from hybridoma T cells
477 expressing the mutant TCRs (Fig. 7F,G).

478 **DISCUSSION**

479 Previously, we and others have shown that mechanical force modulates ligand dissociation, tunes
480 sensitivity to pMHC, amplifies peptide discrimination, and enhances antigen recognition of the
481 TCR (*11-15, 39, 52*). Here we demonstrated that these properties are supported by TCRαβ–CD3
482 *cis*-interactions, as their interference altered TCR–pMHC *trans*-interaction and T cell function.
483 The TCR-CD3 complex is stably held together by noncovalent associations in its transmembrane
484 and extracellular regions. An early study of the complex assembly reported cooperative
485 interactions between the TCRαβ and the CD3 chains through transmembrane segments (*53*).
486 Subsequent NMR chemical shift perturbation experiments required both CD3γε and CD3δε for
487 specific TCRαβ–CD3 interactions, suggesting possible cooperativity (*23*). Here we demonstrated
488 that these ECD interactions are highly cooperative and force-reinforced, manifesting as the
489 formation of a CD3δε'–TCRαβ–CD3γε trimolecular catch bond. The importance of such
490 cooperative *cis*-interaction and its force dependency were demonstrated by the observations that
491 its interferences by antibody and mutations affected TCR–pMHC *trans*-interaction under force
492 (but not in the absence of force) and T cell function as predicted by structural analysis based on
493 CMD/SMD simulations.

494 By integrating our findings with existing data, we formulate a model for TCR triggering to
495 emphasize TCR mechanotransduction and the significance of cooperative TCRαβ–CD3 *cis*-
496 interaction to its mechanoconnectivity, mechanotransduction, and force-induced allostery (Fig.
497 S5). T cells exert force on the TCR via engaged pMHC (*8, 10*) and force triggers T cell signaling
498 (*11, 17*). Regardless of whether exerted extraneously from outside or endogenously from inside

499 the cell, force must be supported by the pMHC–TCRαβ–CD3 serial molecular structure. *In vivo*
500 forces are likely more variable than those experimentally applied to the TCR–pMHC bonds by
501 BFP. The requirement for T cell signaling to be robust, *i.e.*, to trigger intracellular signaling
502 reliably despite the variable external forces, must translate into a requirement for TCR
503 mechanosensing machinery to function reliably in a noisy environment. How may TCRαβ–CD3
504 cooperativity help? Without cooperativity, the bimolecular interaction between TCRαβ and either
505 CD3γε or CD3δε would be much weaker, and hence lasts much shorter, than that between TCR
506 and pMHC, which would prematurely disrupt the mechanoconnectivity and cut off any mechanical
507 communication through ECD interactions, potentially adversely impacting TCR triggering (Fig.
508 S5, *top*). By comparison, with a cooperative trimolecular catch bond, force on one end of the serial
509 molecular structure can be supported by and transmitted through, at least in part, the CD3δε–
510 TCRαβ–CD3γε interactions to prevent the TCRαβ ECD from being pulled away from the CD3
511 ECDs as a result of the much longer CP of TCRαβ than those of the CD3γε and CD3δε (*54*). The
512 intact mechanoconnectivity can therefore sustain possible mechanical communication to allow
513 force-modulated peptide-encoded information to be transmitted from the pMHC through TCRαβ
514 to the CD3 signaling apparatus and to enable force to induce conformational changes in the CD3
515 cytoplasmic domain to trigger signal transduction (*55, 56*) (Fig. S5, *bottom*). Thus, the robustness
516 requirement of TCR triggering may be fulfilled in part by the TCRαβ–CD3 cooperativity.

517 We obtained multiple lines of decisive evidence for cooperativity by direct measurements
518 combined with mathematical modeling, as well as by MD simulations in both the absence and
519 presence of force. All results consistently and definitively show synergy, such that the whole is
520 larger, and lasts longer, than the sum of the parts. The direct measurements of both the pairwise
521 bimolecular, and the cooperative trimolecular, inter-subunit interactions of the TCRαβ–CD3 are

522 remarkable, considering their low affinities and rapid off-rates. Even more remarkable is our
523 observation that the TCRαβ–CD3m pseudo *cis*-interaction forms a catch bond with a comparable
524 force-lifetime relationship to that of the cognate TCR–pMHC *trans*-interaction. However, our
525 results likely underestimate the degree of cooperativity and the level of the trimolecular catch
526 bond. Comparing to their native assembly on the cell membrane, our experiment used an
527 unfavorable "pseudo *cis*" configuration where the TCRαβ was N-terminally linked to a probe to
528 sub-optimally contact CD3s C-terminally linked to an opposite target. The 1:1 ratio mixed CD3γε
529 and CD3δε' were randomly captured by an RBC or bead by biotin-streptavidin coupling.
530 Streptavidin has four biotin binding sites. Two on one side likely bound by the biotinylated RBC
531 membrane proteins and the other two on the opposite side were capable of binding two biotinylated
532 CD3s, generating ≤50% of CD3γε/CD3δε' heterodimers and ≥25% each of CD3δε'/CD3δε' and
533 CD3γε/CD3γε homodimers (*57*) on the target surface. Should a TCRαβ be able to bind
534 synergistically to a CD3γε/CD3δε' heterodimer on the same streptavidin only, not to a CD3γε on
535 one streptavidin and a CD3δε' on another streptavidin (due to the further distance between CD3γε
536 and CD3δε'), the finding of ~47% greater number of whole bonds than the sum of bonds from
537 parts suggests that ~94% of these heterodimers would form trimolecular bonds with the TCRαβ.
538 Thus, TCRαβ–CD3 interactions must occur in 100% as CD3δε'–TCRαβ–CD3γε bond on the T
539 cell surface, especially further considering the CD3γε–CD3δε' interaction (which we observed
540 experimentally and computationally) as well as the structural constraints in the CP and
541 transmembrane regions that better position and orient the two CD3s relative to the TCRαβ on the
542 cell membrane (*26*) than the CD3γε/CD3δε' heterodimer in our experiment. This assertion has
543 been supported by our SMD simulations: Despite the significantly higher forces used and the much

544 shorter bond lifetimes that resulted, the cooperativity index $\Delta\langle t\rangle/\langle t\rangle_{pre}$ shows an order of
545 magnitude higher computational than experimental values.

546 Our SMD simulations revealed structural dynamics and force effects on TCRαβ–CD3
547 interactions, which previous static structural studies (*23-26*) and CMD simulations (*58*) were
548 unable to uncover. We developed occupancy analysis as a novel approach for quantifying the
549 structural features using CMD and SMD results, which evaluates contacts between any residue
550 pairs over a dynamic process in the absence and presence of force. A strength of our approach is
551 the ability to assess all types of atomic-level interactions, including hydrogen bonds, salt bridges,
552 π-π stackings, and hydrophobic interactions. This enabled us to identify a hydrophobic pocket in
553 the trimolecular interaction that would not have been found by only analyzing hydrogen bonds,
554 and provided stronger evidence for the structural mechanism of the cooperativity. The occupancy
555 analysis is highly sensitive for evaluating interactions along a simulated dynamic process and
556 hence especially powerful for evaluating differential contact residues or change thereof from CMD
557 to SMD, enabling us to identify previously unreported and/or force-enhanced contact residues.
558 The relevance of these results has been supported by previous functional experiments, which also
559 supports the validity of our simulations. Previous NMR and CMD studies found 1) Cα AB loop,
560 Cβ helix 3, and Cβ FG loop (*20*) and 2) Cβ helix 3 and Cβ helix 4 (*19*) undergo dynamic changes
561 upon TCR–pMHC engagement, suggesting a TCR triggering mechanism by which ligand binding-
562 induced dynamics may transmit allosterically to CD3 for signal transduction. However, our SMD
563 simulations only found Cβ helix 4 residues to have high RD-OI with CD3 subunits, suggesting
564 their possible relevance to signal transduction.

565 Our findings highlight the importance of ECD interactions within the TCR complex and
566 their cooperativity to the inner workings of the TCR machinery to function as a mechanosensor.

567 Our data offer explanations for the impairment of TCR stability and functionality by mutations on
568 putative interaction sites (*22-24, 27*) and provide opportunities for designing and engineering
569 "better" TCR for immunotherapy applications.
570
571 **METHODS**
572 **Proteins and cells**
573 A biotinylation sequence (GLNDIFEAQKIEWHE) was added to N-terminus of ECD constructs
574 of 2C and 2B4 TCRα and C-terminus of mouse and human CD3γε and CD3δε subunits through
575 PCR (*59*). Proteins were expressed in One Shot™ *E. coli* BL21 (DE3) (Invitrogen) as insoluble
576 inclusion bodies, refolded and purified as previously described (*24*). Inclusion bodies for I-E^k α
577 (with C-terminal biotinylation sequence) and β chains were produced in One Shot™ *E. coli* BL21
578 (DE3), refolded with K5 peptide (ANERADLIAYFKAATKF), and purified as described
579 previously (*60*). SIYR:H2-K^b protein was from the NIH Tetramer Facility at Emory University.
580 For all proteins, purified fractions were biotinylated using a BirA protein ligase kit (Avidity LLC).
581 The biotinylated proteins were further purified by gel filtration (S200, GE Life Sciences) in PBS
582 buffer pH 7.4. The proteins were finally tested for biotinylation efficiency by gel-shift analysis by
583 incubating them in excess streptavidin. Site density of 2B4 TCRαβ coated on RBCs and beads
584 was measured using phycoerythrin (PE)-conjugated anti-mouse Vα11.1, 11.2 mAb (clone RR8-1,
585 BD Pharmingen). Site densities of human CD3γε and CD3δε' in the single coating as well as in
586 the mixed coating at 1:1 ratio were measured using PE-conjugated anti-human CD3ε mAb (clone
587 UCHT1, eBioscience).
588 Mouse $58^{-/-}$ T cell hybridoma cells (*61*) expressing mouse CD3 but not TCRαβ were a
589 generous gift from Dr. Bernard Malissen (Centre d'immunologie de Marseille-Luminy, France).

590 $58^{-/-}$ cells were transfected with mouse 2C or mutant mouse 2B4 TCR constructs through retroviral
591 transduction and cultured as described previously (*24*). The transduced cells were stained with PE
592 anti-mouse CD3ε (clone 145-2C11 or 2C11, eBioscience) and allophycocyanin (APC)-conjugated
593 anti-TCRβ (clone H57-597 or H57, eBioscience) mAbs and sorted for dual expression of CD3 and
594 TCR. The sorted cells were expanded for 6 days and quantified for TCR and CD3ε expression.

595 Fab of anti-TCR Cβ (H57), anti-CD3ε (2C11), anti-TCR Vβ8 (clone F23.1 or F23), and anti-
596 TCRα (clone H28-710 or H28) mAbs were obtained by digesting commercial full-length mAbs
597 using Fab preparation kit (Thermo Fisher 44685). H57 scFv was a generous gift from Johannes
598 Huppa of the Medical University of Vienna (*10*).

599

600 **Micropipette adhesion frequency assay**

601 Our MAF assay for measuring 2D affinity has been described (*28, 29*). Briefly, human RBCs were
602 isolated from whole blood drawn from healthy donors according to a protocol approved by the
603 Institute Review Board of Georgia Institute of Technology. RBCs were biotinylated with
604 controlled concentration of biotin-X-NHS linker (Millipore/Sigma), coated with saturating amount
605 of streptavidin (ThermoFisher), coated with biotinylated proteins of interest, and loaded into
606 different regions of a cell chamber mounted on the stage of an inverted microscope that contained
607 solution streptavidin to block nonspecific binding. A pair of RBCs, each bearing one type of
608 interacting proteins, named as receptor (R) and ligand (L) here, was aspirated by two opposing
609 glass micropipettes (Fig 1B, *top*). The two RBCs were brought into repeated contact-and-retract
610 cycles at constant contact time and area by a piezoelectric translater-driven micropipette. Adhesion
611 frequency (P_a) is the frequency of adhesion events detected by the RBC elongation during
612 retraction. The RBC surface tension was kept low by adjusting the micropipette suction pressure

613 such that pulling by even a single bond would generate visible membrane deflection. For $P_a \leq$
614 90%, adhesion events are mediated by low number of bonds that follow the Poisson distribution
615 that has a single parameter $\langle n \rangle$, which is the average number of bonds formed per contact. P_a and
616 $\langle n \rangle$ are related by:

617 $$P_a = 1 - \exp(-\langle n \rangle) \qquad \langle n \rangle = -\ln(1 - P_a) \qquad (1a,b)$$

618 To relate $\langle n \rangle$ to receptor–ligand binding kinetics requires a model. For all homotypic or
619 heterotypic bimolecular interactions studied in this work, the following probabilistic kinetics
620 equation and solution were used (*28, 29*):

621 $$\frac{d\langle n \rangle}{d(k_{off}t_c)} = m_R m_L A_c K_a - \langle n \rangle \qquad < n > = m_R m_L A_c K_a[1 - \exp(-(k_{off}t_c)] \qquad (2a,b)$$

622 where m_R and m_L (μm^{-2}) are site densities of the interacting molecules on the RBC surfaces, A_c
623 (μm^2) and t_c (s) are contact area and time, K_a (μm^2) and k_{off} (s^{-1}) are 2D affinity and off-rate
624 respectively, m_R and m_L were determined by comparing mean fluorescence intensity (MFI) of
625 targeted proteins stained by saturating amount of fluorescently-tagged antibody to MFI of PE
626 quantitation beads (BD Biosciences). A_c and t_c are controlled parameters during experiments.
627 When $k_{off}t_c$ is much larger than 1, $\langle n \rangle$ approaches steady-state, and the effective 2D binding
628 affinity $A_c K_a$ (μm^4) can be determined by:

629 $$A_c K_a = \frac{\langle n \rangle}{m_R m_L} = \frac{-1}{m_R m_L} \ln(1 - P_a) \qquad (3a,b)$$

630 Since $k_{off} > 10\ s^{-1}$ for all the interactions studied here (Table 1), we used 2-s contact time so that
631 $k_{off} \times t_c > 20$ and P_a reached its steady-state value, and the effective 2D affinity values shown in
632 Fig. 2A were calculated using Equation 3.

633 To account for concurrent binding of TCRαβ to CD3γε and CD3δε' separately and
634 possibly cooperatively, a two-step, two-pathway model was used: In the first step, the TCRαβ
635 interacts with either CD3γε (pathway I, kinetic rates k_1 and k_{-1}) or CD3δε' (pathway II, kinetic

636 rates k_2 and k_{-2}) to form TCRαβ–CD3γε or TCRαβ–CD3δε' bimolecular bonds. In the second step,

637 the TCRαβ–CD3γε bond interacts with CD3δε' (pathway I, kinetic rates k_4 and k_{-4}) or the TCRαβ–

638 CD3δε' bond interacts with CD3γε (pathway II, kinetic rates k_3 and k_{-3}) to form CD3δε'–TCRαβ–

639 CD3γε trimolecular bonds. The probabilistic kinetics equation and steady-state solution are,

640 respectively:

641 $$\frac{d}{dt}\begin{Bmatrix}\langle n\rangle_\gamma\\ \langle n\rangle_\delta\\ \langle n\rangle_{\gamma\delta}\end{Bmatrix}+\begin{bmatrix}m_{\delta\varepsilon'}k_4+k_{-1} & 0 & -k_{-4}\\ 0 & m_{\gamma\varepsilon}k_3+k_{-2} & -k_{-3}\\ -m_{\delta\varepsilon'}k_4 & -m_{\gamma\varepsilon}k_3 & k_{-3}+k_{-4}\end{bmatrix}\begin{Bmatrix}\langle n\rangle_\gamma\\ \langle n\rangle_\delta\\ \langle n\rangle_{\gamma\delta}\end{Bmatrix}=\begin{Bmatrix}m_{\alpha\beta}m_{\gamma\varepsilon}A_{\mathrm{c}}k_1\\ m_{\alpha\beta}m_{\delta\varepsilon'}A_{\mathrm{c}}k_2\\ 0\end{Bmatrix} \quad (4)$$

642 and

643 $$\langle n\rangle_\delta=\frac{m_{\alpha\beta}m_{\gamma\varepsilon}A_{\mathrm{c}}}{m_{\delta\varepsilon'}k_4+k_{-1}}\left[k_1+m_{\delta\varepsilon'}k_{-4}\frac{k_1k_4(m_{\gamma\varepsilon}k_3+k_{-2})+k_2k_3(m_{\delta\varepsilon'}k_4+k_{-1})}{k_{-1}k_{-4}(m_{\gamma\varepsilon}k_3+k_{-2})+k_{-2}k_{-3}(m_{\delta\varepsilon'}k_4+k_{-1})}\right] \quad (5a)$$

644 $$\langle n\rangle_\gamma=\frac{m_{\alpha\beta}m_{\delta\varepsilon'}A_{\mathrm{c}}}{m_{\gamma\varepsilon}k_4+k_{-2}}\left[k_2+m_{\gamma\varepsilon}k_{-3}\frac{k_1k_4(m_{\gamma\varepsilon}k_3+k_{-2})+k_2k_3(m_{\delta\varepsilon'}k_4+k_{-1})}{k_{-1}k_{-4}(m_{\gamma\varepsilon}k_3+k_{-2})+k_{-2}k_{-3}(m_{\delta\varepsilon'}k_4+k_{-1})}\right] \quad (5b)$$

645 $$\langle n\rangle_{\gamma\delta}=m_{\alpha\beta}m_{\gamma\varepsilon}m_{\delta\varepsilon'}A_{\mathrm{c}}\frac{k_1k_4(m_{\gamma\varepsilon}k_3+k_{-2})+k_2k_3(m_{\delta\varepsilon'}k_4+k_{-1})}{k_{-1}k_{-4}(m_{\gamma\varepsilon}k_3+k_{-2})+k_{-2}k_{-3}(m_{\delta\varepsilon'}k_4+k_{-1})} \quad (5c)$$

646 where the subscripts of $\langle n\rangle$ denote average number of bonds of the TCRαβ–CD3γε (γ) or TCRαβ–

647 CD3δε' (δ) bimolecular interaction or the CD3δε'–TCRαβ–CD3γε (δγ) trimolecular interaction.

648 The subscript of m indicates site densities of TCRαβ (αβ), CD3γε (γε), and CD3δε' (δε'). The

649 total TCRαβ bonds with CD3m include three subpopulations:

650 $$\langle n\rangle_{\mathrm{m}}=\langle n\rangle_\gamma+\langle n\rangle_\delta+\langle n\rangle_{\gamma\delta} \quad (6)$$

651 Note that Equation 1 applies to the average number of total bonds, $\langle n\rangle_{\mathrm{m}}$, not its individual

652 components. Cooperative binding takes place in the second step by forming a CD3δε'–TCRαβ–

653 CD3γε trimolecular bond. Letting $k_3 = k_4 = 0$ abolishes the trimolecular bonds and reduces Eqs. 5a

654 and 5b to the steady-state version of Equation 2b for the TCRαβ–CD3γε and TCRαβ–CD3δε'
655 bimolecular bonds, respectively, as expected.
656
657 **Biomembrane force probe (BFP) thermal fluctuation assay**
658 Our BFP thermal fluctuation assay for measuring bond lifetime at the force-free condition has been
659 described (*29, 36*). Briefly, streptavidin-coated probe beads and target beads were prepared using
660 established chemistry and incubated with biotin-tagged proteins of interest. A probe bead was
661 placed on the apex of a biotinylated RBC aspirated by a micropipette, and the target bead or cell
662 aspirated by an opposing micropipette was aligned against the probe bead (Fig. 1E). To block
663 possible biotin–streptavidin interaction between the probe bead and the target bead, the target
664 beads were incubated with streptavidin before adding to the microscope cell chamber that also
665 contained high concentration of solution streptavidin. Due to the softness (0.2 pN/nm) of the RBC
666 membrane, the RBC-probe bead system underwent thermal fluctuation, which generated brief and
667 discontinuous contacts with the target bead positioned near it to allow interaction between the
668 molecules coated on the two sides. The horizontal displacement of the probe bead was monitored
669 by high speed (1000 fps) camera and image analysis. Bond association and dissociation events
670 were identified from reduction and resumption, respectively, of fluctuations in the probe bead
671 displacement. Lifetime was recorded as the duration from fluctuation reduction to resumption. To
672 ensure most interactions represented single-bond events, the site densities of the molecules coated
673 on the beads were adjusted to keep the adhesion frequency below 20%.
674 After setting the right-hand side to zero, Equation 4 can be applied to analyze the two-step,
675 two-pathway dissociation of total bonds that include TCRαβ–CD3γε, TCRαβ–CD3δε', and
676 CD3δε'–TCRαβ–CD3γε bond species. Letting the second-step kinetic rates $k_3 = k_{-3} = k_4 = k_{-4} = 0$

677 abolishes the trimolecular bonds and reduces the homogeneous form of Equation 4 to two
678 uncoupled first-order dissociation kinetic equations for the TCRαβ–CD3γε and TCRαβ–CD3δε'
679 bimolecular bonds, respectively. Their solutions are expressed in terms of survival probabilities:
680 $p_\gamma = \exp(-k_{-1}t)$ and $p_\delta = \exp(-k_{-2}t)$, respectively, which were used to fit the data
681 exemplified in Figure 2D and shown in Figure 2F. The coupled Equation 4 with nonzero second-
682 step kinetic rates was solved numerically using MATLAB, which was used to fit the total bond
683 survival probability data measured from CD3m coating experiments (Fig. 3G, far left).
684

685 **Biomembrane force probe (BFP) force clamp assay**

686 Our BFP force-clamp assay for measuring the force-dependent lifetime of a single molecular bond
687 has been described (*11, 39*). Briefly, the same BFP setup and coating strategy as the thermal
688 fluctuation assay were used in the force-clamp assay except in one set of experiments that
689 measured binding of K5:I-E^k coated on BFP beads to 2B4 TCR expressed on $58^{-/-}$ hybridoma cells
690 (Fig. 1E). The target was brought into contract with the BFP probe for a brief moment, then
691 retracted. If no bond formation was detected (Fig. 1F, *left*), the target movement would turn into
692 the next event cycle; if bond formation was detected, the target would move to a predetermined
693 position and stay there to load the bond with a constant tensile force until spontaneous dissociation
694 to allow measurement of lifetime (Fig. 1F, *right*). Hundreds of such measurements were pooled
695 and grouped into several force bins. Lifetime distributions in each force bin were analyzed using
696 survival probability *vs*. lifetime plots. Mean ± SEM lifetime was plotted *vs.* mean ± SEM force
697 and fitted by a cubic interpolation (Figs. 2E, 3F, 3F) or Gaussian curve (Fig. 2F) for graphing and
698 further statistical analysis. Bootstrapping (1000 samples) of the force-lifetime distributions was
699 used to estimate the mean and SEM of force and lifetimes in each bin more accurately and reliably.

700

701 **Cooperativity analysis**

702 Three types of cooperativity analysis were used to evaluate whether, and if so, the degree by which
703 TCRαβ binds CD3γε and CD3δε synergistically using experimental data, MD simulation results,
704 and mathematical modeling (*40*).

705 Cooperativity analysis in terms of average numbers of bonds: The first type of
706 cooperativity analysis is based on the average numbers of total bonds and two bimolecular bonds,
707 $<n>_m$, $<n>_\gamma$ and $<n>_\delta$, converted from their corresponding adhesion frequencies $P_{a,m}$, $P_{a,\gamma}$, and $P_{a,\delta}$,
708 using Equation 3b. The analysis makes use of the additive property of $<n>$ (but not P_a), such that
709 the whole average bond number ($<n>_m$) from an adhesion mediated by the concurrent binding of
710 two molecular species (CD3γε and CD3δε), if independent, is equal to the sum of average bond
711 numbers ($<n>_\gamma + <n>_\delta$) from two adhesions each mediated by one species (CD3γε or CD3δε) one
712 at a time (*41-43*).

713 After normalization by $m_{\alpha\beta}$ and m_ε, the site densities of TCRαβ and CD3γε or CD3δε, the
714 steady-state $<n>_\gamma/m_{\alpha\beta}m_{\gamma\varepsilon}$ and $<n>_\delta/m_{\alpha\beta}m_{\delta\varepsilon}$ are equal to the effective 2D affinities $A_cK_{a,\gamma}$ and $A_cK_{a,\delta}$,
715 respectively (Equation 3a). If CD3γε and CD3δε bind TCRαβ independently, $<n>_m = <n>_\gamma + <n>_\delta$
716 $= m_{\alpha\beta}m_{\gamma\varepsilon}A_cK_{a,\gamma} + m_{\alpha\beta}m_{\delta\varepsilon}A_cK_{a,\delta}$ at steady-state. Since the anti-CD3ε mAb recognizes both CD3
717 dimers, which were coated on surfaces at a 1:1 ratio, $m_{\gamma\varepsilon} = m_{\delta\varepsilon} = m_\varepsilon/2$, we have $<n>_m/m_{\alpha\beta}m_\varepsilon =$
718 $(A_cK_{a,\gamma} + A_cK_{a,\delta})/2$ at steady-state, i.e. average effective 2D affinity of the two bimolecular bonds.
719 Given the similar values of these two affinities (Fig. S1I), their average is not significantly different
720 from either value ($p > 0.75$, Student-t test). If CD3γε and CD3δε bind cooperatively, however, the
721 normalized average number of total bonds $<n>_m/m_{\alpha\beta}m_\varepsilon$ is expected to be greater than ($<n>_\gamma +$
722 $<n>_\delta)/m_{\alpha\beta}m_\varepsilon$, which is why comparison among normalized $<n>$ values was used to detect

723 cooperativity (Fig. 3B-C). This idea was taken one step further to formulate a criterion and a
724 quantitative index for cooperativity:

725 $$\frac{\Delta\langle n\rangle}{\langle n\rangle_\gamma+\langle n\rangle_\delta}=\frac{\langle n\rangle_\mathrm{m}-\langle n\rangle_\gamma-\langle n\rangle_\delta}{\langle n\rangle_\gamma+\langle n\rangle_\delta}=\frac{2\langle n\rangle_\mathrm{m}/m_{\alpha\beta}m_\varepsilon}{A_\mathrm{c}K_{\mathrm{a},\gamma}+A_\mathrm{c}K_{\mathrm{a},\delta}}-1\begin{cases}=0 & \text{zero cooperativity}\\ >0 & \text{positive cooperativity}\\ <0 & \text{negative cooperativity}\end{cases} \quad (7)$$

726 Zero cooperativity indicates independent binding, while positive or negative cooperativities are
727 respectively defined and quantified by how much the whole is more or less than the sum of parts.
728 Due to the presence of a trimolecular species $\langle n\rangle_{\gamma\delta}$, the average number of each bimolecular bonds
729 ($\langle n\rangle_\gamma$ or $\langle n\rangle_\delta$) formed when TCRαβ was tested against CD3m would not exceed that formed when
730 TCRαβ was tested against CD3γε or CD3δε (*62*). It follows from comparing Eqs. 6 and 7 that
731 $\langle n\rangle_{\gamma\delta} \geq \Delta\langle n\rangle$. Therefore, we could calculate the lower bound for the fraction of trimolecular bonds
732 from the relative increase in average bond number (Fig. 3D). From our data of $\langle n\rangle_\mathrm{m}/(\langle n\rangle_\gamma + \langle n\rangle_\delta)$
733 $- 1 = 47\%$, we determined that the trimolecular bonds to be ≥ 32% (= 47%/147%) of the total
734 bonds.

735 It took multiple sets of experiments over multiple dates to obtain enough data and repeats
736 to assure reliability. To minimize batch-to-batch variations of sample preparation, we measured
737 pairs of $\langle n\rangle_\mathrm{m}$ with either $\langle n\rangle_\gamma$ or $\langle n\rangle_\delta$ in every experiment for differences between TCRαβ
738 binding to dual and single CD3 heterodimer (cf. Fig. 3B for representative data). We repeated the
739 experiment three times to ensure consistence of such differences across different experiments and
740 to generate enough measurements for statistical analysis. To minimize day-to-day variations in
741 different experimental runs, we normalized the $\langle n\rangle_\gamma$ and $\langle n\rangle_\delta$ values by the $\langle n\rangle_\mathrm{m}$ value in each
742 run and then pooled the normalized data for statistical comparison (Fig. 3C). We also determined
743 the cooperativity index in terms of bond numbers according to Equation 7 (Fig. 3D).

744 <u>Cooperativity analysis in terms of average bond lifetimes:</u> The second type of cooperativity

745 analysis used the following equation:

746 $$\frac{\Delta\langle t\rangle}{\left[\frac{\langle n\rangle_\gamma\langle t\rangle_\gamma+\langle n\rangle_\delta\langle t\rangle_\delta}{\langle n\rangle_\gamma+\langle n\rangle_\delta}\right]}=\frac{\langle t\rangle_{\mathrm{m}}}{\left[\frac{\langle n\rangle_\gamma\langle t\rangle_\gamma+\langle n\rangle_\delta\langle t\rangle_\delta}{\langle n\rangle_\gamma+\langle n\rangle_\delta}\right]}-1=\frac{\langle t\rangle_{\mathrm{m}}}{\left[\frac{A_{\mathrm{c}}K_{\mathrm{a},\gamma}\langle t\rangle_\gamma+A_{\mathrm{c}}K_{\mathrm{a},\delta}\langle t\rangle_\delta}{A_{\mathrm{c}}K_{\mathrm{a},\gamma}+A_{\mathrm{c}}K_{\mathrm{a},\delta}}\right]}-1\begin{cases}=0 & \text{zero cooperativity}\\ >0 & \text{positive cooperativity}\\ <0 & \text{negative cooperativity}\end{cases} \quad (8)$$

747 which resembles Equation 7 but replaces the average number of bonds by the average bond

748 lifetimes as the comparison parameter. The <*n*>'s are used as weights for the average lifetimes of

749 TCRαβ bonds with the respective single CD3 subunits. In other words, Equation 8 states that zero,

750 positive and negative cooperativities are respectively defined by whether and, if so, how much the

751 average lifetime formed by whole lasts longer or shorter than the sum of two single species

752 interactions. This was used to test the data shown in Fig. 3E, and the resulting data from the

753 analysis are shown in Fig. 3F.

754 <u>Cooperativity analysis in terms of SMD results:</u> The third type of cooperativity analysis is

755 for bond lifetimes observed in SMD simulations. This is different from the analysis of bond

756 lifetimes measured from BFP experiment because we only simulated a single molecular construct

757 at a time, either TCRαβ–CD3γε or TCRαβ–CD3δε' complexes, or CD3δε'–TCRαβ–CD3γε

758 complex, not the mixed population of two bimolecular and a trimolecular species. To analyze

759 cooperativity between TCR and CD3 subunits, we first calculated the probability density for

760 TCRαβ to dissociate from both CD3γε and CD3δε', assuming that the bimolecular dissociation

761 events in the trimeric complex are independent and that force prevents rebinding upon dissociation.

762 The separate probabilities for TCRαβ not to dissociate from CD3γε and CD3δε', respectively

763 during (0, *t*) are:

764 $$p_\gamma(t) = e^{-t/\langle t\rangle_\gamma} \text{ and } p_\delta(t) = e^{-t/\langle t\rangle_\delta} \quad (9a,b)$$

765 where $\langle t \rangle_\gamma$ and $\langle t \rangle_\delta$ are the expected lifetimes for TCRαβ to dissociate from CD3γε and CD3δε',

766 respectively, estimated using corresponding dimer dissociation times. The cumulative joint

767 probability for TCRαβ to dissociate from both CD3γε and CD3δε' concurrently but independently

768 during (0, *t*) is:

769 $$F(t) = \left[1 - p_\gamma(t)\right] \cdot \left[1 - p_\delta(t)\right] = 1 - e^{-t/\langle t \rangle_\gamma} - e^{-t/\langle t \rangle_\delta} + e^{-t\left(1/\langle t \rangle_\gamma + 1/\langle t \rangle_\delta\right)} \quad (10)$$

770 The corresponding probability density is:

771 $$\rho_{\gamma\delta}(t) = \frac{dF(t)}{dt} = \frac{e^{-t/\langle t \rangle_\gamma}}{\langle t \rangle_\gamma} + \frac{e^{-t/\langle t \rangle_\delta}}{\langle t \rangle_\delta} - \frac{e^{-t\left(1/\langle t \rangle_\gamma + 1/\langle t \rangle_\delta\right)}}{1/\langle t \rangle_\gamma + 1/\langle t \rangle_\delta} \quad (11)$$

772 The average lifetime of the trimolecular bond, assuming no cooperativity, is:

773 $$\langle t \rangle_{\gamma\delta,\mathrm{pred}} = \int_0^\infty t\, \rho_{\gamma\delta}(t) dt = \langle t \rangle_\gamma + \langle t \rangle_\delta - \frac{1}{1/\langle t \rangle_\gamma + 1/\langle t \rangle_\delta} = \langle t \rangle_\gamma + \langle t \rangle_\delta - \frac{\langle t \rangle_\gamma \cdot \langle t \rangle_\delta}{\langle t \rangle_\gamma + \langle t \rangle_\delta}. \quad (12)$$

774 Cooperativity is assessed by comparing the simulated trimolecular bond lifetime $\langle t \rangle_{\delta\gamma,\mathrm{simu}}$ to the

775 trimolecular bond lifetime given by Equation 12, predicted based on the assumption of concurrent

776 but independent dissociation and calculated using the simulated bimolecular bond lifetimes. Thus,

777 the third cooperativity index can be formulated in a similar fashion to Equation 8:

778 $$\frac{\Delta\langle t \rangle}{\langle t \rangle_{\gamma\delta,\mathrm{pred}}} = \frac{\langle t \rangle_{\gamma\delta,\mathrm{simu}} - \langle t \rangle_{\gamma\delta,\mathrm{pred}}}{\langle t \rangle_{\gamma\delta,\mathrm{pred}}} = \frac{\langle t \rangle_{\gamma\delta,\mathrm{simu}}}{\langle t \rangle_{\gamma\delta,\mathrm{pred}}} - 1 \begin{cases} = 0 & \text{zero cooperativity} \\ > 0 & \text{positive cooperativity} \\ < 0 & \text{negative cooperativity} \end{cases} \quad (13)$$

779

780 **Kinetic modeling**

781 The force-dependent lifetimes of TCRαβ bonds with CD3γε, CD3δε, or both all show

782 catch-bond behavior, with biexponentially decaying survival probabilities, suggesting the presence

783 of two bound species, even for the bimolecular interactions. Therefore, for the analysis of

784 bimolecular bond data, we assume that a single bond may dissociate from a weak state or a strong

785 state, similar to previous catch bond models (*63*). The weak state dissociates more rapidly than the

786 strong state with rates $k_{-\mathrm{f}} > k_{-\mathrm{s}}$. Transitions between the two states are described by rates k_{a} and
787 $k_{-\mathrm{a}}$. For analysis of the mixed bond data, the dissociation of both bimolecular TCRαβ–CD3γε and
788 TCRαβ–CD3δε bonds as well as trimolecular CD3δε–TCRαβ–CD3γε bonds also follows the two-
789 state catch-bond model. The reaction diagrams for all models are depicted in Fig. S3A.

790 The force dependence of all kinetic rates follows Bell's equation (*45*):

791 $$k_{\mathrm{i,j}} = k_{\mathrm{i,j}}^{0} \exp\left(\frac{f \cdot x_{\mathrm{i,j}}}{k_{\mathrm{B}} T}\right) \tag{14}$$

792 where the subscripts i (-f, -s, a or -a) and j (γ, δ or m) denote different kinetic rates of different
793 complexes, the superscript 0 denotes the respective zero-force kinetic rate, $x_{\mathrm{i,j}}$ denotes distance to
794 the transition state, or width of the energy well that traps the system in the bound state, k_{B} is
795 Boltzmann constant, and T is absolute temperature. This two-state catch-bond model is able to
796 recapitulate the averaged bond lifetime as well as the biexponentially distributed bond survival
797 probabilities. Here, the zero-force fast dissociation rates $k_{-\mathrm{f}}^{0}$ for the two biomolecular bonds were
798 obtained from thermal fluctuation experiment, while the remaining parameters were evaluated
799 from globally fitting the model to the force-lifetime distributions as a whole via maximum
800 likelihood estimation (MLE). The initial proportions of the two states a $t = 0$ were determined from
801 the ratios of the kinetic rates assuming equilibrium. A two-step optimization procedure was
802 employed to minimize the MLE, which explored a large parameter space by Differential Evolution
803 (DE) to obtain an approximate solution, followed by L-BFGS to hone in the minimum (Fig. S2B-
804 D). The kinetic rates *vs*. force are depicted in Fig. S2E-G with the Bell parameters summarized in
805 Fig. S2I. The standard deviation for each parameter was obtained by inversing the Hessian matrix
806 at the MLE to obtain the approximate covariance matrix whose diagonal entries correspond to the
807 variance of the fitted parameters.

808

809 **Molecular dynamics simulations**

810 Molecular constructs: All simulations were based on the cryoEM structure (PDB ID: 6JXR)(*26*).
811 The TCRαβ, CD3γε, and CD3δε' were truncated near the CPs between extracellular and
812 intercellular regions, leaving the complete TCR ECD in its trimeric assembly. The TCRαβ ECD
813 contained α chain Gly22-Glu237 and β chain Val26-Glu269. The CD3γε and CD3δε' ECDs were
814 obtained by truncating γ chain after Cys107, ε chain of CD3γε after Asn121, δ chain after Glu98,
815 and ε' chain of CD3δε' after Glu124. To minimize potential trimming effects, all chain ends were
816 modified to prevent the exposure of charged residues. An acetyl group was added in front of the
817 N-terminus and an N-methyl amine group caps the C-terminus of every chain. All hydrogen atoms,
818 as well as any missing atoms, were added back through Gromacs utilities (*26*). The disulfide bonds
819 in the original cryoEM structure were preserved through Gromacs interactive S-S bridge selection
820 procedures (*26*). The resulting CD3δε'–TCR–CD3γε trimeric complex represents the fully
821 assembled ECD. Then, two partial assemblies were generated by removing CD3γε, CD3δε', and
822 TCR individually from the complete ECD, achieving three dimeric complexes (TCR–CD3γε,
823 TCR–CD3δε', and CD3γε–CD3δε', respectively).

824 Unit cell preparation: Unit cells were built to enclose the molecular systems to be simulated
825 in a physiologically-appropriate and thermodynamically-favorable state. The initial structures
826 were oriented and centered within optimized orthorhombic cells, which accommodated the
827 physical extensions in all directions with a ≥1.6 nm buffering zone apart from the box sides to
828 ensure the protein was well-isolated. The molecules in unit cells were solvated using the TIP3P
829 water model (*64*). The negative charges were counterbalanced using sodium ions, then tuning the
830 ionic strength to ~150 mM with sodium chloride. To further prepare the system

831 thermodynamically, energy unfavorable close contacts were eliminated through the steepest
832 descent and conjugate gradient energy minimization cycles. While restraining the heavy atoms in
833 macromolecules, the unit cell was brought to the suitable ensemble employing 200 ps velocity
834 rescaling simulation to adjust the temperature and 200 ps Berendsen Barostat simulation to correct
835 the pressure (300 K, 1.01325 bar). After releasing the heavy-atom restraints, the systems were
836 considered ready for subsequent equilibration and production runs.

837 Conventional molecular dynamics: CMD simulations were performed using GROMACS
838 (version 2019.6) (*65-67*) under recent AMBER99SB*-ILDNP force field with improved helix-coil
839 transitional and side-chain torsional dynamics (*68*). From previously prepared unit cells, the set of
840 initial velocities were randomly sampled from the Maxwell-Boltzmann distribution. The
841 molecular trajectories were self-evolved under the leap-frog algorithm for integrating Newton's
842 law of motion over 2 fs time period. For CMD, the individual simulations runs were executed
843 under periodic boundary conditions to sample the NVT ensemble with corresponding constant
844 volumes (CD3δε'–TCR–CD3γε: 12.5 × 10.8 × 9.9 nm^3; TCR–CD3γε: 12.6 × 9.8 × 8.6 nm^3; TCR–
845 CD3δε': 11.9 × 10.3 × 9.2 nm^3; CD3γε–CD3δε': 11.5 × 8.1 × 8.0 nm^3) and a constant temperature
846 of 300 K. The neighborhood lists were refreshed every 10 steps based on the buffered Verlet
847 scheme with a 1.2 nm non-bonded cutoff for Coulomb and van der Waals interactions. The long-
848 range potentials of electrostatic interactions were computed using the Particle Ewald Mesh
849 summation method. The simulated trajectories were 200 ns for every system, consisting of a 50-
850 ns equilibration and a 150-ns production run. The conformational snapshots per 0.1 ns during the
851 production stage were extracted and analyzed to obtain ensemble averages.

852 Steered molecular dynamics: In SMD simulations, the well-equilibrated conformations
853 from free dynamics at 100 ns were used as initial configurations. They were prepared according

854 to the Unit cell preparation section but with a 20-nm of box length to accommodate the molecular
855 extension and separation under external pulling. The external forces with constant magnitudes or
856 constant velocities along fixed direction (z-axis) were added to the trimeric and dimeric
857 complexes. The C-termini of CD3ε chains (NME residues) were fixed to mimic the anchor effect
858 of their transmembrane domains. Clamp or ramp forces were applied to the N-terminus of the TCR
859 α chain (ACE residues) to accelerate the dissociation. To pull the CD3δε'–TCR–CD3γε trimeric
860 complex, two points at the base of the CD3s was used to anchor the complete ECD. To pull the
861 TCR–CD3γε and TCR–CD3δε' dimeric complexes, by comparison, only a single anchor spot at
862 the end of ε chain ECD was used. For force-clamp simulations, five independent trajectories under
863 100, 125, 150, 175, and 200 pN were produced for each of the two dimeric systems; three
864 independent runs under 150, 175, and 200 pN were executed for the trimeric complex as
865 simulations at smaller clamp forces were aborted due to the inability to observe dissociation after
866 exceedingly long time. For force-ramping simulations, 70 pN/nm pseudo springs were linked to α
867 chain ACE residues with free ends departing away in z-direction at 1 nm/ns. Five repeats each on
868 three ECD complexes were conducted to assess corresponding rupture forces statistically.
869
870 **Occupancy analysis**
871 Several variations of occupancy analysis were employed to dynamically evaluate the extent of a
872 particular residue in contact with its binding partner throughout the simulation. At the particular
873 timestamp i, the residue being analyzed is defined to be in contact (denoted o_i=1) if the center of
874 mass of this residue is within 4 Å of any atoms of its binding partner; otherwise, it is not in touch
875 (denoted o_i=0). The occupancy index (%) indicates the fraction of time in contact during a given
876 period, as $\sum_{i=0}^{N} o_i/N$, where N is total number of analyzed frames.

877 Residue-to-redisue occupancy index (RR-OI): By setting residues inside a subunit as a
878 reference group, this occupancy analysis quantifies the extent of dynamic interaction over a period
879 of each residue from one subunit with every residue from the other subunit. Thus, RR-OI evaluated
880 the level of any pairwise protein–protein interaction, thereby forming a correlation matrix where
881 the columns index the residues from one subunit, the rows index the residues from the other subunit,
882 and the elements denote values of particular residue-to-residue occupancy indices.

883 Residue-to-domain cocupancy index (RD-OI): This occupancy analysis quantifies each
884 residue against all residues within its binding partner, using the entire subunit as the reference
885 group instead of its individual residues. RD-OI is usually smaller than the sum of RR-OI over the
886 binding domain because the residue in question may simultaneously be in contact with multiple
887 residues in the domain under consideration, and these contact periods can only be counted once.

888 Domain-to-domain occupancy index (DD-OI): The occupancy analysis takes averages of
889 RD-OI over interacting residues (*i.e.,* positive terms) inside a domain to examine its overall
890 binding tendency against the other domain.

891 Furthermore, to examine how cooperativity impacts the interface between TCR ECD
892 subunits, different occupancy analyses were performed to distinguish bimolecular and trimolecular
893 dynamics. To examine how force impacts the interface, different occupancy analyses were
894 performed to compare force-free and force-clamp dynamics.

895

896 **Statistical analysis**

897 Applied statistical approaches were specified in figure legends. Mean with standard error of the
898 mean (SEM) was used for reporting the confidence level of absolute mean value; Mean with
899 standard deviation (SD) was used for comparisons among experimental conditions; Box and

whiskers plots were used to display population scattering level. Depending on the nature of the data, linear regression, cubic interpolation, or Gaussian distribution were used in curve fitting, with the uncertainty range showing confidence interval or SEM. Errors of predicted values from models were calculated from the error of input data with error propagation. Student's t-test based analysis assuming paired/unpaired, parametric/nonparametric distributions was used between two groups depending on the condition of each case. Analysis of variance (ANOVA) was used when comparing more than two objects. One sample t-test was used when evaluating cooperativity indexes comparing to zero.

910 **ACKNOWLEDGEMENTS**

911 This work was supported by NIH grants R01GM124489 (to M.K. and C.Z.) and U01 CA214354
912 (to C.Z. and M.K.). The MD simulations were supported by an NSF award (MCA08X014) in
913 advanced computing infrastructure for U.S. and performed in the Extreme Science and
914 Engineering Discovery Environment (XSEDE). Cell sorting/flow cytometry technologies were
915 provided by NYU Langone's Cytometry and Cell Sorting Laboratory, which is supported in part
916 by NIH grant P30CA016087. SIYR:H2-K^b protein was made by the NIH Tetramer Core Facility
917 at Emory University. We thank Larissa Doudy for technical assistance, Johannes Huppa for
918 providing the H57 scFv, and Bernard Malissen for providing mouse $58^{-/-}$ T cell hybridoma cells.

919

920

921 **AUTHOR CONTRIBUTIONS**

922 C.Z. and C.G. conceived the study; C.Z. and M.K. directed the study; Z.Y., C.G., and A.N.
923 performed experiments; P.C. performed simulations; P.C. and A.N. performed structural analysis;
924 A.N, S.B, and D.G produced proteins; S.T. analyzed data using mathematical models; Z.Y., P.C.,
925 A.N., M.K., and C.Z. analyzed data and wrote the paper with contributions from other authors.

926

927 **STATEMENT OF COMPETING INTERESTS**

928 The authors have no competing interests to declare.

929

930 REFERENCES

931

932 1. A. H. Courtney, W. L. Lo, A. Weiss, TCR Signaling: Mechanisms of Initiation and
933 Propagation. *Trends Biochem Sci* **43**, 108-123 (2018).

934 2. C. Zhu, W. Chen, J. Lou, W. Rittase, K. Li, Mechanosensing through immunoreceptors.
935 *Nat Immunol* **20**, 1269-1278 (2019).

936 3. R. A. Mariuzza, P. Agnihotri, J. Orban, The structural basis of T-cell receptor (TCR)
937 activation: An enduring enigma. *J Biol Chem* **295**, 914-925 (2020).

938 4. B. Alarcon, D. Gil, P. Delgado, W. W. Schamel, Initiation of TCR signaling: regulation
939 within CD3 dimers. *Immunol Rev* **191**, 38-46 (2003).

940 5. D. Moogk, A. Natarajan, M. Krogsgaard, T cell receptor signal transduction: affinity, force
941 and conformational change. *Current Opinion in Chemical Engineering* **19**, 43-50 (2018).

942 6. P. A. van der Merwe, O. Dushek, Mechanisms for T cell receptor triggering. *Nat Rev*
943 *Immunol* **11**, 47-55 (2011).

944 7. A. L. Lanz *et al.*, Allosteric activation of T cell antigen receptor signaling by quaternary
945 structure relaxation. *Cell Rep* **36**, 109375 (2021).

946 8. Y. Liu *et al.*, DNA-based nanoparticle tension sensors reveal that T-cell receptors transmit
947 defined pN forces to their antigens for enhanced fidelity. *Proc Natl Acad Sci U S A* **113**,
948 5610-5615 (2016).

949 9. R. Ma *et al.*, DNA probes that store mechanical information reveal transient piconewton
950 forces applied by T cells. *Proc Natl Acad Sci U S A* **116**, 16949-16954 (2019).

951 10. J. Gohring *et al.*, Temporal analysis of T-cell receptor-imposed forces via quantitative
952 single molecule FRET measurements. *Nat Commun* **12**, 2502 (2021).

953 11. B. Liu, W. Chen, B. D. Evavold, C. Zhu, Accumulation of dynamic catch bonds between
954 TCR and agonist peptide-MHC triggers T cell signaling. *Cell* **157**, 357-368 (2014).

955 12. J. Hong *et al.*, Force-Regulated In Situ TCR-Peptide-Bound MHC Class II Kinetics
956 Determine Functions of CD4+ T Cells. *J Immunol* **195**, 3557-3564 (2015).

957 13. P. Wu *et al.*, Mechano-regulation of Peptide-MHC Class I Conformations Determines TCR
958 Antigen Recognition. *Mol Cell* **73**, 1015-1027 e1017 (2019).

959 14. D. K. Das *et al.*, Force-dependent transition in the T-cell receptor beta-subunit
960 allosterically regulates peptide discrimination and pMHC bond lifetime. *Proc Natl Acad*
961 *Sci U S A* **112**, 1517-1522 (2015).

962 15. L. V. Sibener *et al.*, Isolation of a Structural Mechanism for Uncoupling T Cell Receptor
963 Signaling from Peptide-MHC Binding. *Cell* **174**, 672-687 e627 (2018).

964 16. S. T. Kim *et al.*, The alphabeta T cell receptor is an anisotropic mechanosensor. *J Biol*
965 *Chem* **284**, 31028-31037 (2009).

966 17. Y. Feng *et al.*, Mechanosensing drives acuity of alphabeta T-cell recognition. *Proc Natl*
967 *Acad Sci U S A* **114**, E8204-E8213 (2017).

968 18. S. Pryshchep, V. I. Zarnitsyna, J. Hong, B. D. Evavold, C. Zhu, Accumulation of serial
969 forces on TCR and CD8 frequently applied by agonist antigenic peptides embedded in
970 MHC molecules triggers calcium in T cells. *J Immunol* **193**, 68-76 (2014).

971 19. K. Natarajan *et al.*, An allosteric site in the T-cell receptor Cbeta domain plays a critical
972 signalling role. *Nat Commun* **8**, 15260 (2017).

973 20. S. Rangarajan *et al.*, Peptide-MHC (pMHC) binding to a human antiviral T cell receptor
974 induces long-range allosteric communication between pMHC- and CD3-binding sites. *J*
975 *Biol Chem* **293**, 15991-16005 (2018).

976 21. B. Knapp, P. A. van der Merwe, O. Dushek, C. M. Deane, MHC binding affects the
977 dynamics of different T-cell receptors in different ways. *PLoS Comput Biol* **15**, e1007338
978 (2019).

979 22. M. S. Kuhns *et al.*, Evidence for a functional sidedness to the alphabetaTCR. *Proc Natl*
980 *Acad Sci U S A* **107**, 5094-5099 (2010).

981 23. Y. He *et al.*, Identification of the Docking Site for CD3 on the T Cell Receptor beta Chain
982 by Solution NMR. *J Biol Chem* **290**, 19796-19805 (2015).

983 24. A. Natarajan *et al.*, Structural Model of the Extracellular Assembly of the TCR-CD3
984 Complex. *Cell Rep* **14**, 2833-2845 (2016).

985 25. M. E. Birnbaum *et al.*, Molecular architecture of the alphabeta T cell receptor-CD3
986 complex. *Proc Natl Acad Sci U S A* **111**, 17576-17581 (2014).

987 26. Dong *et al.*, Structural basis of assembly of the human T cell receptor-CD3 complex.
988 *Nature* **573**, 546-552 (2019).

989 27. M. S. Kuhns, M. M. Davis, Disruption of extracellular interactions impairs T cell receptor-
990 CD3 complex stability and signaling. *Immunity* **26**, 357-369 (2007).

991 28. S. E. Chesla, P. Selvaraj, C. Zhu, Measuring two-dimensional receptor-ligand binding
992 kinetics by micropipette. *Biophysical journal* **75**, 1553-1572 (1998).

993 29. J. Huang *et al.*, The kinetics of two-dimensional TCR and pMHC interactions determine
994 T-cell responsiveness. *Nature* **464**, 932-936 (2010).

995 30. E. Evans, K. Ritchie, R. Merkel, Sensitive force technique to probe molecular adhesion
996 and structural linkages at biological interfaces. *Biophys J* **68**, 2580-2587 (1995).

997 31. J. Wang *et al.*, Atomic structure of an alphabeta T cell receptor (TCR) heterodimer in
998 complex with an anti-TCR fab fragment derived from a mitogenic antibody. *The EMBO*
999 *journal* **17**, 10-26 (1998).

1000 32. R. A. Fernandes *et al.*, T cell receptors are structures capable of initiating signaling in the
1001 absence of large conformational rearrangements. *J Biol Chem* **287**, 13324-13335 (2012).

1002 33. S. A. Richman *et al.*, Structural features of T cell receptor variable regions that enhance
1003 domain stability and enable expression as single-chain ValphaVbeta fragments. *Molecular*
1004 *immunology* **46**, 902-916 (2009).

1005 34. M. Krogsgaard *et al.*, Evidence that structural rearrangements and/or flexibility during
1006 TCR binding can contribute to T cell activation. *Mol Cell* **12**, 1367-1378 (2003).

1007 35. E. W. Newell *et al.*, Structural basis of specificity and cross-reactivity in T cell receptors
1008 specific for cytochrome c-I-E(k). *J Immunol* **186**, 5823-5832 (2011).

1009 36. W. Chen, E. A. Evans, R. P. McEver, C. Zhu, Monitoring receptor-ligand interactions
1010 between surfaces by thermal fluctuations. *Biophysical journal* **94**, 694-701 (2008).

1011 37. B. Liu *et al.*, 2D TCR-pMHC-CD8 kinetics determines T-cell responses in a self-antigen-
1012 specific TCR system. *Eur J Immunol* **44**, 239-250 (2014).

1013 38. K. Li, X. Cheng, A. Tilevik, S. J. Davis, C. Zhu, In situ and in silico kinetic analyses of
1014 programmed cell death-1 (PD-1) receptor, programmed cell death ligands, and B7-1
1015 protein interaction network. *J Biol Chem* **292**, 6799-6809 (2017).

1016 39. J. Hong *et al.*, A TCR mechanotransduction signaling loop induces negative selection in
1017 the thymus. *Nat Immunol* **19**, 1379-1390 (2018).

1018 40. K. Li *et al.*, PD-1 suppresses TCR-CD8 cooperativity during T-cell antigen recognition.
1019 *Nature communications* **12**, 2746 (2021).

1020 41. C. Zhu, T. E. Williams, Modeling concurrent binding of multiple molecular species in cell
1021 adhesion. *Biophys J* **79**, 1850-1857 (2000).

1022 42. T. E. Williams, P. Selvaraj, C. Zhu, Concurrent binding to multiple ligands: kinetic rates
1023 of CD16b for membrane-bound IgG1 and IgG2. *Biophys J* **79**, 1858-1866 (2000).

1024 43. T. E. Williams, S. Nagarajan, P. Selvaraj, C. Zhu, Concurrent and independent binding of
1025 Fcgamma receptors IIa and IIIb to surface-bound IgG. *Biophys J* **79**, 1867-1875 (2000).

1026 44. E. Evans, A. Leung, V. Heinrich, C. Zhu, Mechanical switching and coupling between two
1027 dissociation pathways in a P-selectin adhesion bond. *Proceedings of the National Academy*
1028 *of Sciences* **101**, 11281-11286 (2004).

1029 45. G. I. Bell, Models for the specific adhesion of cells to cells. *Science* **200**, 618-627 (1978).

1030 46. M. Karplus, G. A. Petsko, Molecular dynamics simulations in biology. *Nature* **347**, 631-
1031 639 (1990).

1032 47. S. Izrailev *et al.*, in *Computational molecular dynamics: challenges, methods, ideas*.
1033 (Springer, 1999), pp. 39-65.

1034 48. A. Natarajan *et al.*, In situ cell-surface conformation of the TCR-CD3
1035 signaling complex. *bioRxiv*, 2022.2002.2007.479368 (2022).

1036 49. N. Martinez-Martin *et al.*, Cooperativity between T cell receptor complexes revealed by
1037 conformational mutants of CD3epsilon. *Sci Signal* **2**, ra43 (2009).

1038 50. T. Beddoe *et al.*, Antigen ligation triggers a conformational change within the constant
1039 domain of the alphabeta T cell receptor. *Immunity* **30**, 777-788 (2009).

1040 51. A. Alcover, B. Alarcon, V. Di Bartolo, Cell Biology of T Cell Receptor Expression and
1041 Regulation. *Annu Rev Immunol* **36**, 103-125 (2018).

1042 52. X. Zhao *et al.*, Tuning T cell receptor sensitivity through catch bond engineering. *Science*
1043 **376**, eabl5282 (2022).

1044 53. N. Manolios, F. Letourneur, J. Bonifacino, R. Klausner, Pairwise, cooperative and
1045 inhibitory interactions describe the assembly and probable structure of the T-cell antigen
1046 receptor. *The EMBO journal* **10**, 1643-1651 (1991).

1047 54. J. h. Wang, E. L. Reinherz, The structural basis of αβ T-lineage immune recognition: TCR
1048 docking topologies, mechanotransduction, and co-receptor function. *Immunological*
1049 *reviews* **250**, 102-119 (2012).

1050 55. D. Gil, W. W. Schamel, M. Montoya, F. Sanchez-Madrid, B. Alarcon, Recruitment of Nck
1051 by CD3 epsilon reveals a ligand-induced conformational change essential for T cell
1052 receptor signaling and synapse formation. *Cell* **109**, 901-912 (2002).

1053 56. C. Xu *et al.*, Regulation of T cell receptor activation by dynamic membrane binding of the
1054 CD3epsilon cytoplasmic tyrosine-based motif. *Cell* **135**, 702-713 (2008).

1055 57. K. K. Sarangapani, B. T. Marshall, R. P. McEver, C. Zhu, Molecular stiffness of selectins.
1056 *J Biol Chem* **286**, 9567-9576 (2011).

1057 58. E. N. Bingol, O. Sercinoglu, P. Ozbek, Unraveling the Allosteric Communication
1058 Mechanisms in T-Cell Receptor-Peptide-Loaded Major Histocompatibility Complex
1059 Dynamics Using Molecular Dynamics Simulations: An Approach Based on Dynamic

1060 Cross Correlation Maps and Residue Interaction Energy Calculations. *J Chem Inf Model*
1061 **61**, 2444-2453 (2021).

1062 59. L. Kjer-Nielsen *et al.*, Crystal structure of the human T cell receptor CD3 epsilon gamma
1063 heterodimer complexed to the therapeutic mAb OKT3. *Proc Natl Acad Sci U S A* **101**,
1064 7675-7680 (2004).

1065 60. M. Krogsgaard *et al.*, Agonist/endogenous peptide-MHC heterodimers drive T cell
1066 activation and sensitivity. *Nature* **434**, 238-243 (2005).

1067 61. F. Letourneur, B. Malissen, Derivation of a T cell hybridoma variant deprived of functional
1068 T cell receptor α and β chain transcripts reveals a nonfunctional α-mRNA of BW5147
1069 origin. *European journal of immunology* **19**, 2269-2274 (1989).

1070 62. V. F. Fiore, L. Ju, Y. Chen, C. Zhu, T. H. Barker, Dynamic catch of a Thy-1-
1071 alpha5beta1+syndecan-4 trimolecular complex. *Nat Commun* **5**, 4886 (2014).

1072 63. C. D. Buckley *et al.*, Cell adhesion. The minimal cadherin-catenin complex binds to actin
1073 filaments under force. *Science* **346**, 1254211 (2014).

1074 64. W. L. Jorgensen, J. Chandrasekhar, J. D. Madura, R. W. Impey, M. L. Klein, Comparison
1075 of simple potential functions for simulating liquid water. *The Journal of chemical physics*
1076 **79**, 926-935 (1983).

1077 65. U. R. Shrestha *et al.*, Generation of the configurational ensemble of an intrinsically
1078 disordered protein from unbiased molecular dynamics simulation. *Proc Natl Acad Sci U S*
1079 *A* **116**, 20446-20452 (2019).

1080 66. B. Hess, C. Kutzner, D. Van Der Spoel, E. Lindahl, GROMACS 4: algorithms for highly
1081 efficient, load-balanced, and scalable molecular simulation. *Journal of chemical theory*
1082 *and computation* **4**, 435-447 (2008).

1083 67. M. J. Abraham *et al.*, GROMACS: High performance molecular simulations through
1084 multi-level parallelism from laptops to supercomputers. *SoftwareX* **1**, 19-25 (2015).

1085 68. K. Lindorff-Larsen *et al.*, Improved side-chain torsion potentials for the Amber ff99SB
1086 protein force field. *Proteins* **78**, 1950-1958 (2010).

1087 69. F. Eisenhaber, P. Lijnzaad, P. Argos, C. Sander, M. Scharf, The double cubic lattice
1088 method: efficient approaches to numerical integration of surface area and volume and to
1089 dot surface contouring of molecular assemblies. *Journal of computational chemistry* **16**,
1090 273-284 (1995).

1091 70. O. Trott, A. J. Olson, AutoDock Vina: improving the speed and accuracy of docking with
1092 a new scoring function, efficient optimization, and multithreading. *J Comput Chem* **31**,
1093 455-461 (2010).

1094

1095 **FIGURE LEGENDS**
1096
1097 **Figure 1. Antibody blocking of TCRαβ–CD3 interactions impairs TCR–pMHC interaction**
1098 **and reduces T cell function. (A)** TCR complexed with anti-TCR Cβ (H57) Fab (*left*) or anti-
1099 CD3ε (2C11) Fab (*right*) modelled by docking the cocrystal structures of H57 Fab bound to N15
1100 TCRαβ (1NFD) (*31*) and of 2C11 Fab bound to CD3ε (3R08) (*32*) onto the cryoEM structure of
1101 the TCR-CD3 complex (6JXR). **(B)** Schematics of MAF assay setup and coating strategies for
1102 interacting molecules. Biotinylated RBCs were sequentially incubated with streptavidin (SA) and
1103 biotinylated proteins. For TCRαβ–CD3γε interaction (*C*), the 2C TCRαβ was N-terminally-
1104 biotinylated and the mouse CD3γε ECDs were C-terminally-biotinylated (*upper*). For TCR–
1105 pMHC interaction (*D*), 2C TCR was expressed on T hybridoma cells and pMHC (SIYR:H2-K^b)
1106 was C-terminally-biotinylated (*lower*). **(C)** Adhesion frequency (P_a) of TCRαβ–CD3γε interaction
1107 in the presence (*red*) or absence (*blue*) of 10 μg/ml indicated full mAbs or scFv. **(D)** P_a of TCR–
1108 pMHC interaction in the presence (*red*) or absence (*blue*) of 10 μg/ml indicated mAb fragments.
1109 **(E)** Schematics of BFP setup and coating strategy for interacting molecules. Streptavidin-coated
1110 probe beads were incubated with biotinylated proteins similar to (*A*). **(F)** Representative force *vs.*
1111 time traces from BFP force-clamp assay exemplifying a no-binding (*left*) and a binding (*right*)
1112 event. The force plateau highlighted in red indicates bond lifetime under a constant clamp force.
1113 **(G)** TCR–pMHC bond lifetime at 10 pN measured in the presence (*red*) or absence (*blue*) of 10
1114 μg/ml of H57 Fab or scFv. (**H**) IL-2 production (area under the dose-dependent curve, AUC) of
1115 hybridoma expressing 2C TCR activated by SIYR:H-$2K^b$ complexes displayed on EL-4 cells in
1116 the presence (*red*) or absence (*blue*) of 5 μg/ml of indicated mAb Fab, normalized by the result
1117 without Fab blocking. As an anti-TCRα mAb, H28 does not bind TCRαβ assembled in the TCR
1118 complex. Data in (*C*), (*D*), (*G*), and (*H*) are presented as mean ± SME, with (*C*) and (*D*) showing
1119 results of >3 paired experiments for each mAb, (*G*) showing results of 54-64 measurements at
1120 forces ranging in 9-11 pN, response curves in (*H*) summarizing combined result from eight peptide
1121 (SIYR) concentrations in triplicates ranging from 0-1 mM. Significance was assessed by unpaired
1122 parametric t-test in (*B*), (*C*), and (*H*). Difference between absence of blocking (*blue*) and any
1123 treatment conditions (*red*) in (*H*) was hightly significant ($p<0.0001$).
1124

1125 **Figure 2. 2D kinetic analysis of TCRαβ–CD3 ECD interactions reveal low affinity, fast-**
1126 **dissociation, and catch bond formation. (A)** Effective 2D affinities (A_cK_a) of indicated
1127 interactions measured by the MAF assay. For TCRαβ–CD3 interactions, the 2B4 TCRαβ ECD
1128 was N-terminally-biotinylated, and the human CD3γε or CD3δε ECDs were C-terminally-
1129 biotinylated; for CD3γε–CD3δε interaction, CD3 subunits were linked through N-terminus on one
1130 surface and C-terminus on the opposite surface, with setup as Fig. 1B (*upper*). For TCR–pMHC
1131 interaction, 2B4 TCR complex was expressed on T hybridoma cells, and pMHC (K5:I-E^k) was C-
1132 terminally-biotinylated, setup as Fig. 1B (*lower*). **(B)** Representative survival probability from a
1133 BFP thermal fluctuation experiment, shown as a normalized ln(# of events with a lifetime >t) *vs.* t
1134 plot for lifetimes of CD3γε–CD3δε bonds, with setup as Fig. 1E (*upper*). Dissociation off-rate
1135 (k_{off}) was solved as the negative slope of the linear fit to data. **(C)** Off-rates of indicated interactions
1136 analyzed using the method in (*B*). **(D)** Effective 2D on-rates ($A_ck_{on} = A_cK_a \times k_{off}$) calculated based
1137 on the values in (*A*) and (*C*). **(E)** Bond lifetime *vs*. force data (point) and cubic interpolation (curve)
1138 of TCRαβ–CD3γε (blue triangle), TCRαβ–CD3δε (orange square), and CD3γε–CD3δε (black
1139 circle) interactions, with setup as in Fig. 1E (*upper*). **(F)** Bond lifetime *vs*. force data (point) and
1140 Gaussian fit (curve) of 2B4 TCR–K5:I-E^k interaction, with setup as Fig. 1E (*lower*). Data are
1141 presented as mean ± SEM in (*A*) and (*C*-*F*), with >3 experiments in (*A*), linear fit to 69
1142 measurements with 95% confidence interval in (*B*), linear fit to 69-136 measurements to generate
1143 k_{off} values in (*C*), Gaussian error propagation for error bars in (*D*), and 33-111 measurements per
1144 force bin in (*E*) and (*F*).
1145

1146 **Figure 3. Cooperative binding of CD3γε and CD3δε to TCRαβ enhances TCR stability. (A)**
1147 Coating schematics of RBCs or BFP beads for cooperativity analysis. One surface was coated with
1148 N-terminally-biotinylated 2B4 TCRαβ (*right*) and the opposing surface was coated with either C-
1149 terminally-biotinylated human CD3γε, CD3δε, or both in a 1:1 molar ratio ("CD3m") (*left*). **(B)**
1150 Normalized average number of bonds data from one representative experiment of TCRαβ binding
1151 to CD3γε or CD3m and to CD3δε or CD3m. Data were measured using the same TCRαβ-bearing
1152 RBC to test a pair of RBCs bearing single or dual CD3 species in random order. **(C)** Pooled average
1153 number of bonds data from three independent experiments as in (*B*). Result further normalized by
1154 the mean $\langle n \rangle_m / m_{\alpha\beta} m_{\varepsilon}$ in each experiment to remove the inter-experimental variations, revealing
1155 significant lower values of TCRαβ binding to CD3γε, CD3δε, and their predicted average (<CD3>)
1156 than TCRαβ binding to CD3m. **(D)** Cooperativity index of average number of bonds. The
1157 significantly positive mean value demonstrates 47% enhanced binding resulted from cooperativity.
1158 **(E)** Lifetime of TCRαβ–CD3m bonds *vs.* force data (red circle) and model prediction based on
1159 fitted kinetic rates (curves). The data of TCRαβ–CD3γε (blue triangle) and TCRαβ–CD3δε (orange
1160 square) bond lifetimes from Fig. 2E are replotted along with the model fits (blue and orange
1161 curves), which are significantly ($p < 0.05$) shorter-lived that the TCRαβ–CD3m bonds. **(F)**
1162 Measured and model-predicted (curves) cooperativity index of lifetime, relative difference
1163 between the average lifetime of the whole bonds of TCRαβ with concurrently presented dual CD3s
1164 ($\langle t \rangle_m$) and the weighted sum of average lifetimes of TCRαβ–CD3γε and TCRαβ–CD3δε bonds
1165 measured separately ($\langle t \rangle_\gamma$ and $\langle t \rangle_\delta$). The weights were fractions of bond formation based on the
1166 affinities of TCRαβ–CD3γε and TCRαβ–CD3δε interactions. **(G)** Representative survival
1167 probabilities of TCRαβ–CD3γε, TCRαβ–CD3δε, and TCRαβ–CD3m bonds at indicated force bins
1168 shown as ln(# of events with a lifetime $>t$) *vs.* t plots. **(H)** The probability of CD3δε–TCRαβ–
1169 CD3γε trimolecular bond formation as a function of force and lifetime. Data points in (*B*) and (*C*)
1170 are presented as mean ± SD; data in (*D*) are presented as box plot with the whisker showing min
1171 to max; data points in (*E*) and (*F*) are presented as mean ± SEM of 33-111 measurements with
1172 fitted curves presented as mean ± SE. Significance was assessed in (*B*), (*C*) and (*E*) by unpaired
1173 nonparametric t-test and in (*D*) and (*F*) by one sample t-test comparion to zero.
1174

1175 **Figure 4. MD simulations reveal cooperative ECD interaction among TCR-CD3 subunits.**
1176 **(A)** Molecular constructs for MD simulations: the trimeric ECDs are extracted from the cryoEM
1177 structure (6JXR) (*26*), the dimeric ECDs are modeled by removing either CD3 from the trimer.
1178 **(B-C)** Mean ± SEM of contact areas (*B*), defined by solvent accessible surface area algorithm (*69*),
1179 and interaction energies (*C*), quantified using Autodock empirical scoring functions (*70*), between
1180 TCRαβ–CD3γε (blue), TCRαβ–CD3δε (orange), CD3γε–CD3δε (green) complexes calculated
1181 from dimeric (*left*) and trimeric (*middle*) CMD simulations, as well as TCRαβ–CD3γε + TCRαβ–
1182 CD3δε (pink), and TCRαβ–CD3γε + TCRαβ–CD3δε + CD3γε–CD3δε' (red) from trimeric CMD
1183 simulations (*right*). ****$p \leq 0.0001$ between any two groups by unpaired t tests. **(D)** SMD
1184 simulated minimum distance *vs.* time of TCRαβ–CD3δε (orange), TCRαβ–CD3γε (blue), TCRαβ–
1185 CD3γε–CD3δε (red) bonds under 175 pN force. The sudden departure of the trajectory from
1186 baseline signified dissociation time at which defined bond lifetime. **(E)** Bond lifetime *vs.* clamp-
1187 force relationship for the indicated ECD bonds. **(F)** Cooperativity index as relative difference
1188 between the simulated CD3δε–TCRαβ–CD3γε trimolecular bond lifetime and its predicted value
1189 using the TCRαβ–CD3γε and TCRαβ–CD3δε bimolecular bond lifetimes simulated separately,
1190 assuming concurrent but independent dissociation of TCRαβ from both CD3s. *$p \leq 0.05$ by one
1191 sample t-test for comparison with zero.
1192
1193

1194 **Figure 5. Structural basis of force-enhanced cooperative TCRαβ-CD3 interactions. (A-B)**
1195 Sum (*A*) or difference (*B*) of the TCRαβ to CD3γε and CD3δε' RR-OI matrices from SMD and
1196 CMD results, showing only non-zero values, with the residue abbreviations and indices labeled on
1197 the right (CD3γε and CD3δε') and bottom (TCRαβ). Top and left sidebars show the cumulative
1198 values over columns or rows respectively, indicating the overall interacting level of each residue
1199 and its residing secondary structure. **(C)** RD-OI value *vs.* index of TCRα and β residue contacting
1200 CD3 ECDs, and of CD3 γ, ε, ε' and δ residue contacting TCRαβ ECDs in the TCRαβ–CD3γε
1201 (blue), TCRαβ–CD3δε' (orange) and CD3δε'–TCRαβ–CD3γε (red) complexes. **(D)** Force-free
1202 *vs.* force-clamp DD-OI plots of CD3γ, ε, ε' or δ chain (identified by symbol) contacting TCRαβ
1203 (*top*), or TCRα or β chains contacting CD3γε and/or CD3δε' (*bottom*). Points of force-clamp (*x*)
1204 and force-free (*y*) DD-OI values calculated using dimeric (labeled as "*γε*", "*δε'*") or trimeric
1205 (labeled as "*tri*") complex are labeled by the same symbol and connected by dashed line(s). The
1206 force-free results were derived from CMD trajectory. The force-clamp results for TCRαβ–CD3γε
1207 and TCRαβ–CD3δε' were averaged across five independent SMD trajectories under 100, 125, 150,
1208 175, and 200 pN; the force-clamp results for CD3δε'–TCRαβ–CD3γε were averaged across three
1209 independent SMD trajectories under 150, 175, and 200 pN**.**
1210
1211

1212 **Figure 6. Critical residues for TCRαβ-CD3 cooperative interaction. (A-C)** Snapshots of
1213 contact residues identified by 175-pN force-clamp SMD of the trimeric complex mapped onto the
1214 zoom-in views of the CD3δε'–TCRαβ–CD3γε (*A*), TCRαβ–CD3γε (*B*), and TCRαβ–CD3δε' (*C*)
1215 interfaces. CD3δε' and CD3γε are removed from (*B*) and (*C*) for visual clarity. **(D-F)** Snapshots
1216 of contact residues identified by 175-pN force-clamp SMD of the corresponding dimeric complex
1217 mapped onto the zoom-in views of the TCRαβ–CD3γε (*E*) and TCRαβ–CD3δε' (*F*) interfaces, and
1218 a model created by combining the two partial snapshots of the CD3δε'–TCRαβ–CD3γε interface
1219 from the two dimeric snapshots (*D*). The sidechains of the contact residues with OI greater than
1220 90% (*A,D*), 85% (*B,E*), and 40% (*C,F*) are shown. Individual residues and their contacting
1221 sidechains are colored in white for TCRα, salmon for TCRβ, magenta for ε of CD3γε, yellow for
1222 γ of CD3γε, cyan for ε' of CD3δε', and green for δ of CD3δε'. **(G)** A zoom-out view to put the
1223 close-up snapshots in (*A*-*C*) into context of a full ECD assembly of TCRαβ (gray), CD3γε (light
1224 blue), and CD3δε' (orange): the center pocket (black circle), the TCRαβ–CD3γε contact residue
1225 patch (blue circle), and the TCRαβ–CD3δε' contact residue patch (orange circle) are arranged as
1226 an inverted triangle in this top-down view. The high combined ΣRD-OI of both in CMD and SMD
1227 (sum > 1.5) contact residues are shown using sticks colored white to red gradually. A dashed circle
1228 below the center pocket indicates the contact residue patch at the CD3γε–CD3δε' interface
1229 (sidechains not shown). **(H, I)** ΔRD-OI (differential RD-OI) (*H*) and root-mean-square fluctuation
1230 (RMSF, *I*) profiles between SMD and CMD are shown by colors (red for positive, blue for negative,
1231 and white for zero values) and mapped onto the same top-down view as (*G*) but using different
1232 representations. The sidechains of same high combined ΣRD-OI residues as (*G*) are highlighted in
1233 (*H*). The residues' absolute RMSF values are represented by the thickness of the protein backbone
1234 in (I). See also Video S11.

1235

1236 **Figure 7. Mutating high occupancy residues at the TCRαβ–CD3 interfaces impacts TCR–**
1237 **pMHC force-dependent bond lifetime and T cell function, but not 2D affinity at zero force.**
1238 **(A)** Sequence alignment of TCRβ regions from various species indicates the conserved high
1239 occupancy residues and the mutation strategies. **(B)** Structure of 2B4 TCR with the locations of
1240 mutated residues indicated. **(C)** Effective 2D affinities (A_cK_a) of WT 2B4 TCR or indicated
1241 mutants interacting with K5:I-E^k. **(D)** Bond lifetime *vs*. force data (point) and cubic interpolation
1242 (curve) of hybridoma expressing WT 2B4 TCR or indicated mutants interacting with K5:I-E^k. **(E)**
1243 The peak lifetime in (*D*). **(F)** Area under the dose response curve (AUC) of IL-2 cytokine
1244 production by hybridoma expressing WT 2B4 TCR and indicated mutants activated by K5:I-E^k
1245 complexes displayed on CHO cells, normalized by the AUC value of the WT 2B4 TCR. **(G)**
1246 Correlation between the peak lifetime and IL-2 cytokine production. Data in (*C*), (*D*), (*F*) and (*G*)
1247 *y*-axis are presented as mean ± SME; the fitted curves in (*D*), (*E*), and (*G*) *x*-axis are presented as
1248 mean ± SE. (*C*) shows results of >3 measurements. (*D*) shows results of 610 (NP), 355 (WT), and
1249 584 (GK) measurements. Response curves in (*F*) summarize combined results from twelve peptide
1250 (SIYR) concentrations in triplicates ranging from 0-100 μM. Error bars in (*E*) are solved from the
1251 curve fitting in (*D*) and in (*F*) from AUC fitting. Differences between WT and any of the two
1252 mutants was highly significant ($p<0.0001$) by unpaired parametric t-test.
1253

1254

Chain	Secondary regions	Residue	Expression change, functional effects	Reference documenting interaction
TCRα	AB loop	K148	-- (*32*)	
	DE loop	R185	- (*32*), calcium flux reduction (*27*)	CryoEM (*26*)
		S186	--- (*32*), change in activation (*27*)	CryoEM (*26*)
		M187	-- (*32*), calcium flux reduction (*27*)	
TCRβ	CC' loop	N181	--- (*32*)	CryoEM (*26*)
		G182	-- (*32*), IL-2 reduction(*24*)	
	Helix 4	S216	+ (*32*)	NMR (*23*)
		T218	-- (*32*)	NMR (*23*)
		F219	--- (*32*)	NMR (*23, 24*)
	Helix 4-F strand	P223	- (*32*), IL-2 increase (*24*)	
		R224	--- (*32*)	NMR (*23, 24*)
		N225	IL-2 reduction (*24*)	NMR (*23, 24*)
		H226	-- (*32*), IL-2 reduction (*24*)	CryoEM (*26*)
	G strand	I253		CryoEM (*26*), NMR (*23*)
		S255	+ (*32*), IL-2 increase (*48*)	Crosslink (*48*)
		E257		Crosslink (*48*)
		W259	+ (*32*), IL-2 increase (*48*)	Crosslink (*48*)
CD3δ	AB loop	L29	--- (*32*)	CryoEM (*26*)
		E30	--- (*32*)	CryoEM (*26*)
		D31	--- (*32*)	
		R32	--- (*32*)	
	EF loop	K62	-- (*32*)	CryoEM (*26*)
		I64	-- (*32*)	CryoEM (*26*)
CD3ε	CD loop	N62	-- (*32*)	
		D63	- (*32*)	
		K64	- (*32*)	
	FG loop	L90	- (*32*)	CryoEM (*26*)
		E91	- (*32*)	
	H strand	R115	--- (*32*), impaired activation & IL-2 (*49*)	
		(R117)	--- (*32*), impaired activation & IL-2 (*49*)	
CD3γ	AB loop	Y34	+ (*32*)	
		D35		CryoEM (*26*)
		Y36	--- (*32*)	CryoEM (*26*)
		Q37	-- (*32*)	
		E38	--- (*32*)	
		G40	--- (*32*)	

Table 1 | Summary of high occupancy residues, their prior identification, and reported roles. High occupancy residues (RD-OI ≥ 0.8 identified by CD3δε'–TCRαβ–CD3γε force-clamp SMD) are listed by the TCR chains, secondary regions, and residue numbers to which they belong, together with their prior structural identification and reported functional roles. Residues in brackets have RD-OI ≥ 0.7. Residues in red have increased their occupancy indices by ≥0.3 in the presence of force.

Figure 1

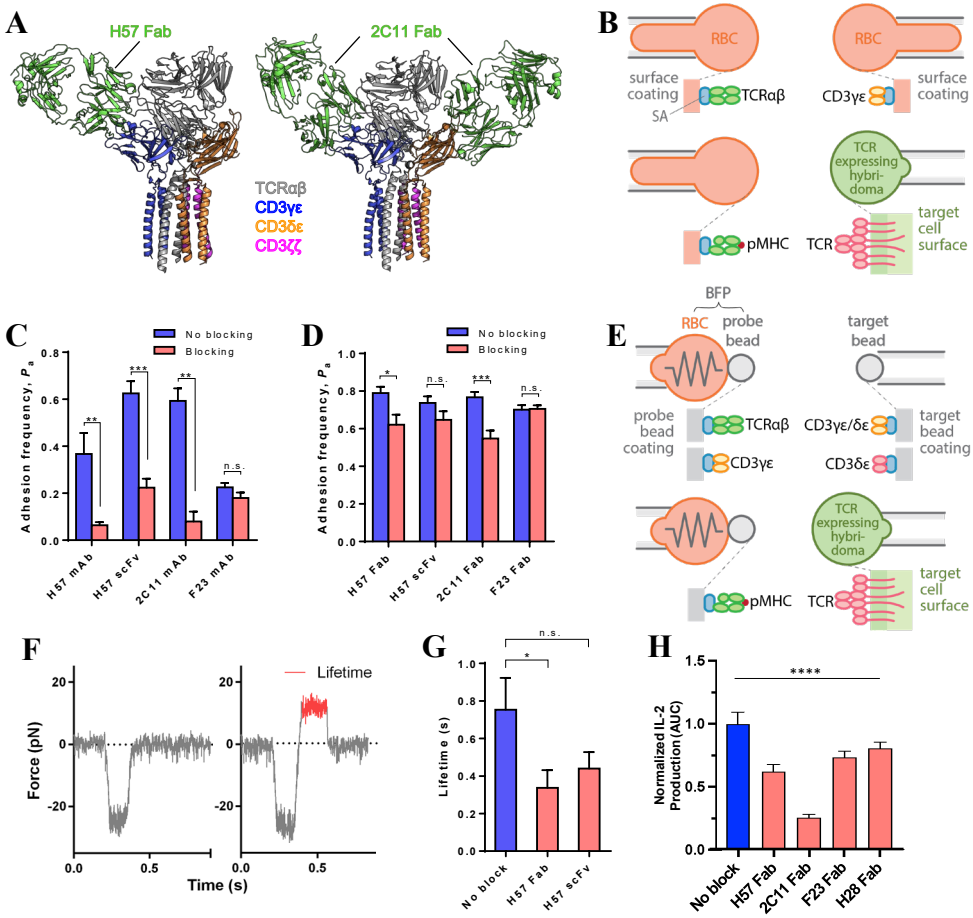
A
H57 Fab
2C11 Fab
TCRαβ
CD3γε
CD3δε
CD3ζζ
B
RBC
surface coating
SA
TCRαβ
CD3γε
TCR expressing hybri-doma
pMHC
TCR
target cell surface
C
No blocking
Blocking
Adhesion frequency, P_a
H57 mAb
H57 scFv
2C11 mAb
F23 mAb
D
H57 Fab
H57 scFv
2C11 Fab
F23 Fab
E
BFP
probe bead
target bead
probe bead coating
CD3γε/δε
CD3δε
target bead coating
F
Lifetime
Force (pN)
Time (s)
G
Lifetime (s)
No block
H57 Fab
H57 scFv
H
Normalized IL-2 Production (AUC)
No block
H57 Fab
2C11 Fab
F23 Fab
H28 Fab

Figure 2

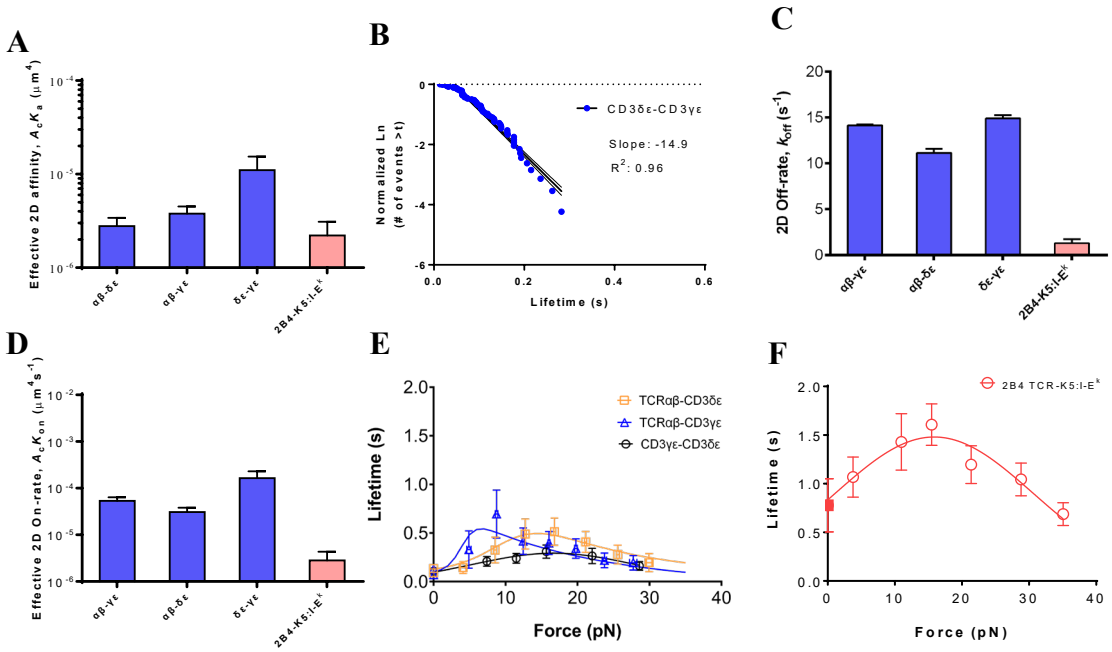
A
Effective 2D affinity, A_cK_a (μm^4)
αβ-δε
αβ-γε
δε-γε
2B4-K5:I-E^k
B
Normalized Ln (# of events > t)
CD3δε-CD3γε
Slope: -14.9
R^2: 0.96
Lifetime (s)
C
2D Off-rate, k_{off} (s^{-1})
αβ-γε
αβ-δε
δε-γε
2B4-K5:I-E^k
D
Effective 2D On-rate, A_cK_{on} ($\mu m^4 s^{-1}$)
αβ-γε
αβ-δε
δε-γε
2B4-K5:I-E^k
E
Lifetime (s)
TCRαβ-CD3δε
TCRαβ-CD3γε
CD3γε-CD3δε
Force (pN)
F
Lifetime (s)
2B4 TCR-K5:I-E^k
Force (pN)

Figure 3

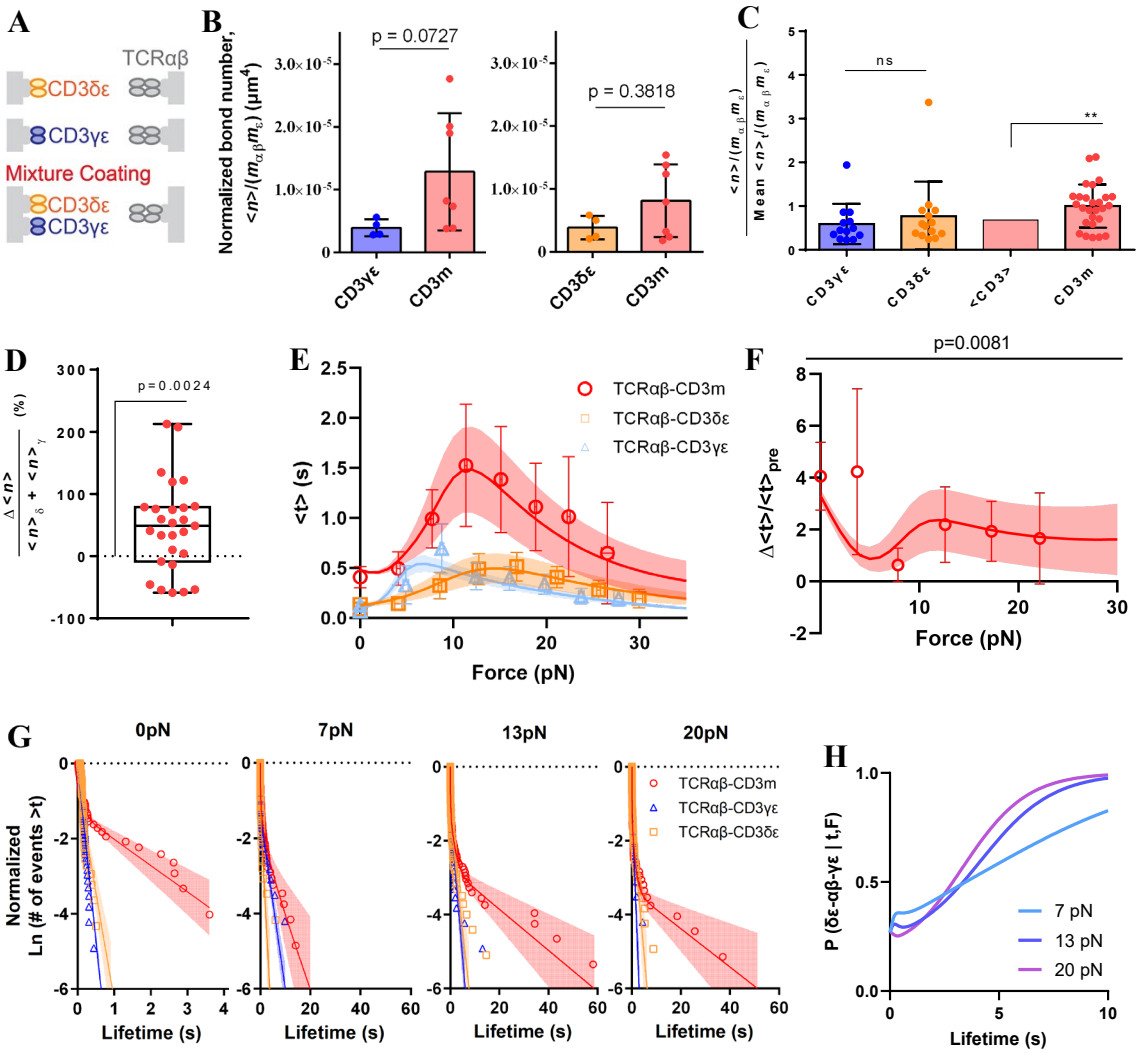
A
TCRαβ
CD3δε
CD3γε
Mixture Coating
CD3δε
CD3γε
B
Normalized bond number, <n>/(mαβmε) (μm4)
p = 0.0727
p = 0.3818
CD3γε
CD3m
CD3δε
CD3m
C
<n>/(mαβmε) / Mean <n>γ/(mαβmε)
ns
**
CD3γε
CD3δε
<CD3>
CD3m
D
Δ<n> / <n>δ + <n>γ (%)
p=0.0024
E
<t> (s)
TCRαβ-CD3m
TCRαβ-CD3δε
TCRαβ-CD3γε
Force (pN)
F
p=0.0081
Δ<t>/<t>pre
Force (pN)
G
0pN
7pN
13pN
20pN
Normalized Ln (# of events >t)
TCRαβ-CD3m
TCRαβ-CD3γε
TCRαβ-CD3δε
Lifetime (s)
H
P (δε-αβ-γε | t,F)
7 pN
13 pN
20 pN
Lifetime (s)

Figure 4

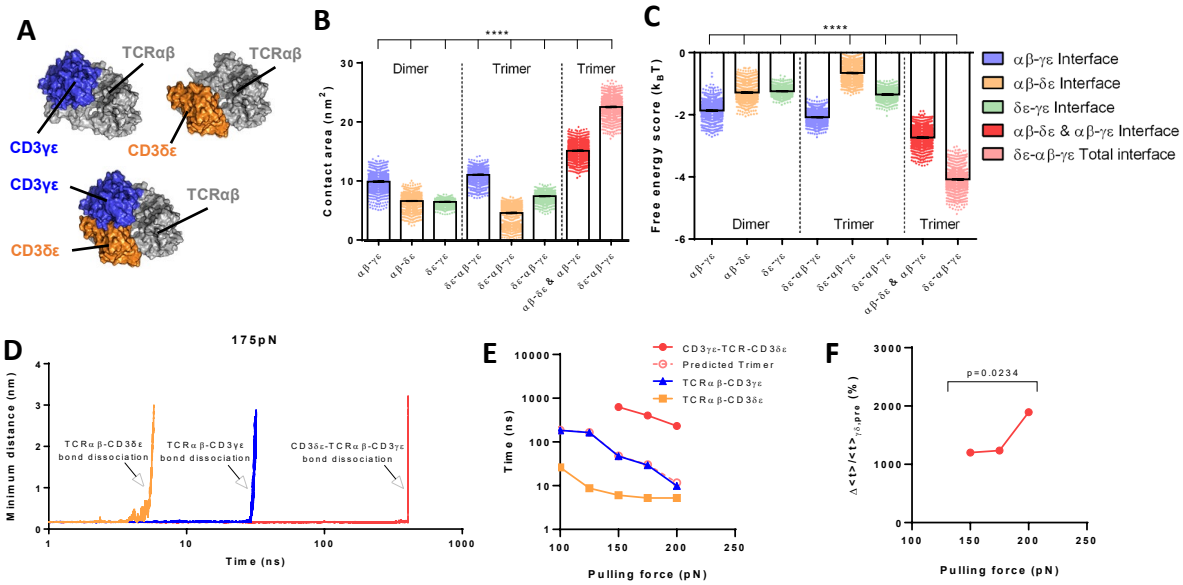
A
TCRαβ
TCRαβ
CD3γε
CD3δε
CD3γε
TCRαβ
CD3δε
B
****
Dimer
Trimer
Trimer
Contact area (nm²)
αβ-γε
αβ-δε
δε-γε
δε-αβ-γε
δε-αβ-γε
δε-αβ-γε
αβ-δε & αβ-γε
δε-αβ-γε
C
****
Free energy score (k_BT)
Dimer
Trimer
Trimer
αβ-γε Interface
αβ-δε Interface
δε-γε Interface
αβ-δε & αβ-γε Interface
δε-αβ-γε Total interface
D
175pN
Minimum distance (nm)
TCRαβ-CD3δε bond dissociation
TCRαβ-CD3γε bond dissociation
CD3δε-TCRαβ-CD3γε bond dissociation
Time (ns)
E
CD3γε-TCR-CD3δε
Predicted Trimer
TCRαβ-CD3γε
TCRαβ-CD3δε
Time (ns)
Pulling force (pN)
F
p=0.0234
Δ<t>/<t>γε,pre (%)
Pulling force (pN)

Figure 5

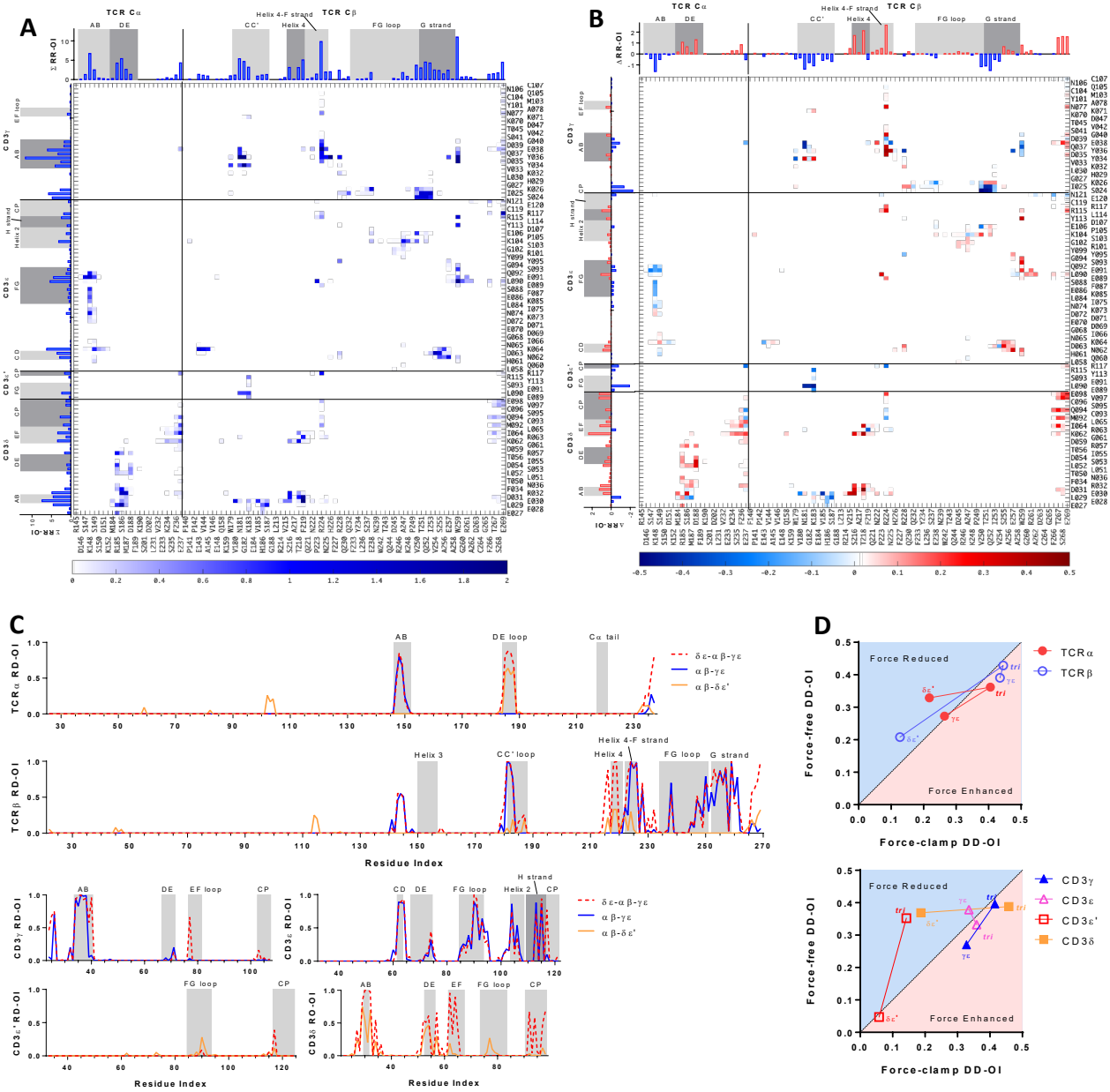
A
B
C
D
TCR Cα
TCR Cβ
Helix 4-F strand
AB
DE
CC'
Helix 4
FG loop
G strand
Σ RR-OI
ΔRR-OI
CD3γ
CD3ε
CD3ε'
CD3δ
EF loop
H strand
Helix 2
CP
FG
CD
EF
TCRα RD-OI
TCRβ RD-OI
CD3γ RD-OI
CD3ε RD-OI
CD3ε' RD-OI
CD3δ RO-OI
Cα tail
Helix 3
CC' loop
Residue Index
δε-αβ-γε
αβ-γε
αβ-δε'
Force Reduced
Force Enhanced
Force-free DD-OI
Force-clamp DD-OI
TCRα
TCRβ
CD3γ
CD3ε
CD3ε'
CD3δ
tri
γε
δε'

Figure 6

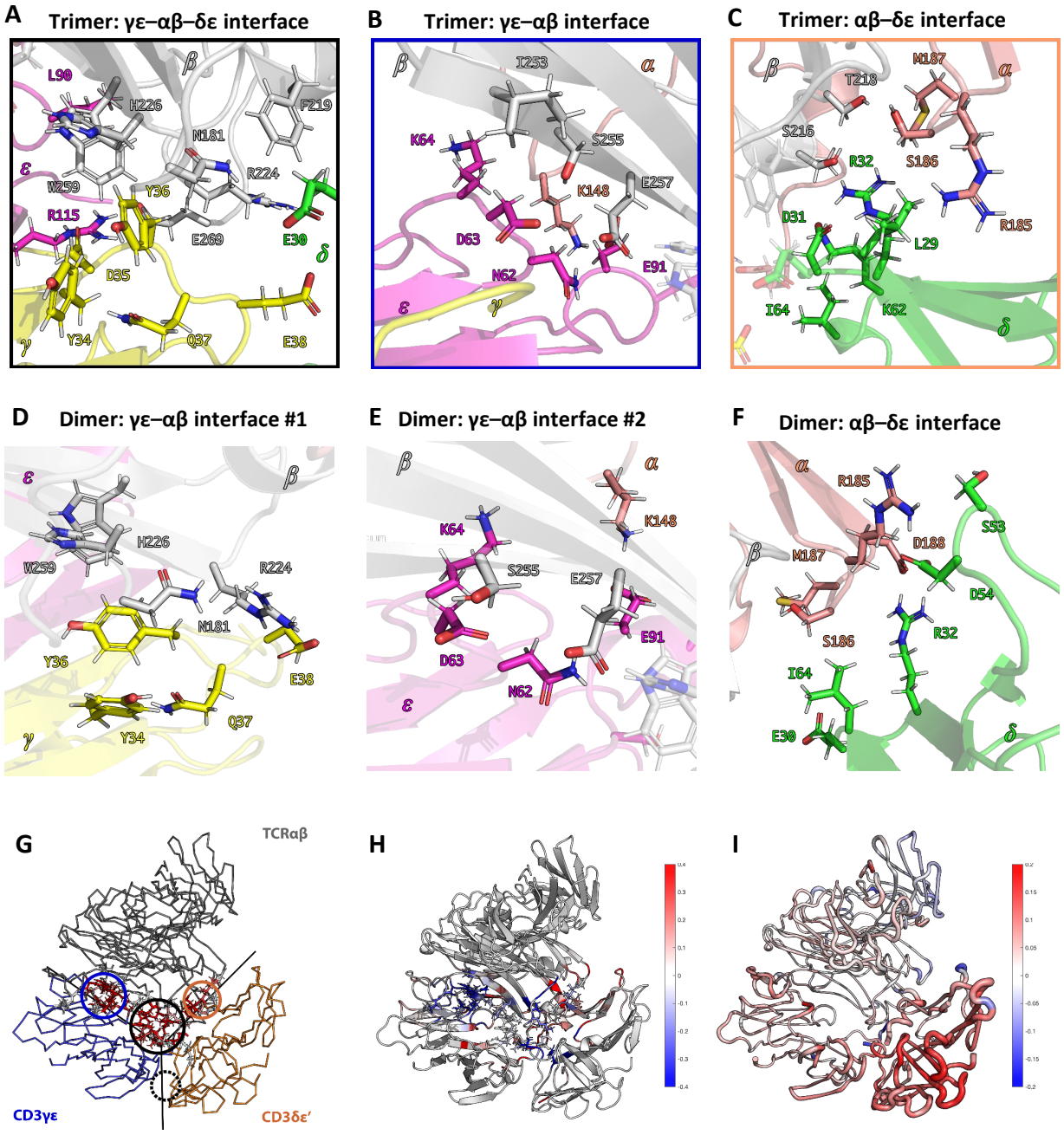
A
Trimer: γε–αβ–δε interface
L90
H226
F219
N181
R224
W259
Y36
R115
E269
E30
D35
Y34
Q37
E38
B
Trimer: γε–αβ interface
I253
K64
S255
K148
E257
D63
N62
E91
C
Trimer: αβ–δε interface
M187
T218
S216
R32
S186
D31
R185
L29
I64
K62
D
Dimer: γε–αβ interface #1
H226
W259
R224
N181
Y36
E38
Q37
Y34
E
Dimer: γε–αβ interface #2
K64
K148
S255
E257
E91
D63
N62
F
Dimer: αβ–δε interface
R185
S53
D188
M187
D54
S186
R32
I64
E30
G
TCRαβ
CD3γε
CD3δε′
H
I

Figure 7

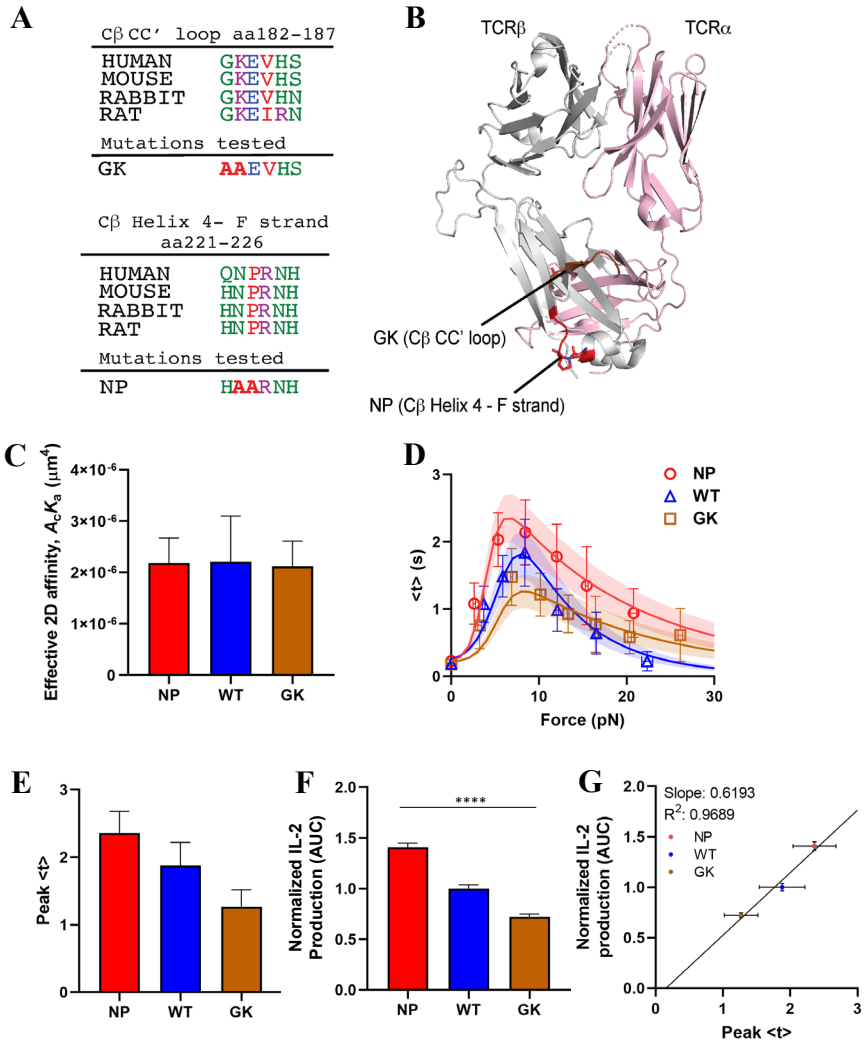
A
Cβ CC' loop aa182-187
HUMAN GKEVHS
MOUSE GKEVHS
RABBIT GKEVHN
RAT GKEIRN
Mutations tested
GK AAEVHS
Cβ Helix 4- F strand aa221-226
HUMAN QNPRNH
MOUSE HNPRNH
RABBIT HNPRNH
RAT HNPRNH
Mutations tested
NP HAARNH
B
TCRβ
TCRα
GK (Cβ CC' loop)
NP (Cβ Helix 4 - F strand)
C
Effective 2D affinity, A_cK_a (μm^4)
4×10^{-6}
3×10^{-6}
2×10^{-6}
1×10^{-6}
0
NP
WT
GK
D
NP
WT
GK
<t> (s)
Force (pN)
E
Peak <t>
NP
WT
GK
F
Normalized IL-2 Production (AUC)
****
NP
WT
GK
G
Slope: 0.6193
R^2: 0.9689
NP
WT
GK
Normalized IL-2 production (AUC)
Peak <t>

Supplementary Figures with Legends

Cooperative ectodomain interaction among TCRαβ, CD3γε and CD3δε

Zhou Yuan[1-3†], Peiwen Cong[1,3†], Aswin Natarajan[4†], Chenghao Ge[1,3†], Stefano Travaglino[1,3], Saikiran Beesam[4], Danielle Grazette[4], Michelle Krogsgaard[4‡], Cheng Zhu[1-3‡]

[1]Wallace H. Coulter Department of Biomedical Engineering, [2]Georgia W. Woodruff School of Mechanical Engineering, [3]Petit Institute for Bioengineering and Bioscience, Georgia Institute of Technology, Atlanta, GA, USA; [4]Laura and Isaac Perlmutter Cancer Center and Department of Pathology, New York University Grossman School of Medicine, New York, NY, USA

[†]These authors contributed equally.

[‡]Contact: cheng.zhu@bme.gatech.edu, 1-404-894-3269 or Michelle.Krogsgaard@nyulangone.org, 212-263-9266,

[a]Present address: Amgen Inc., One Amgen Center Dr., Thousand Oaks, CA, USA

Figure S1

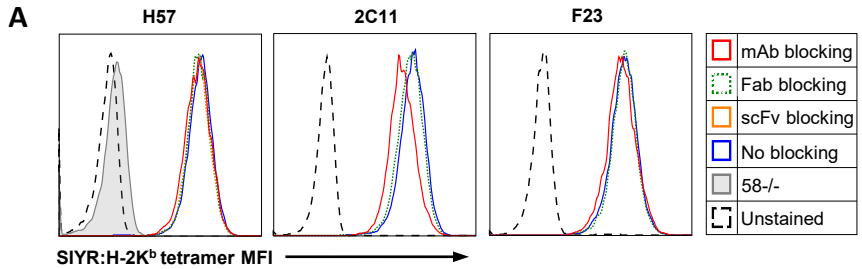

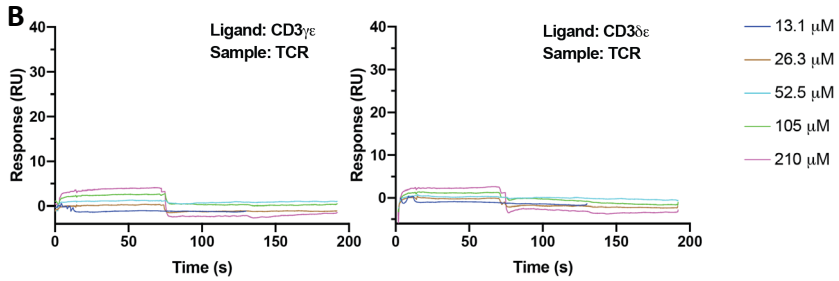

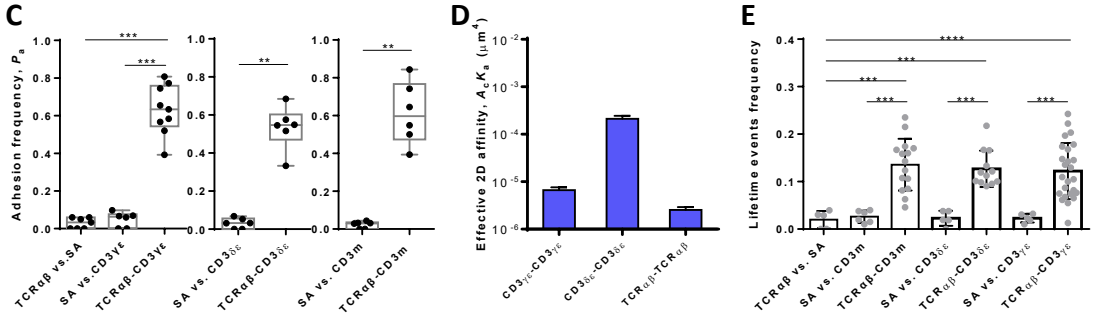

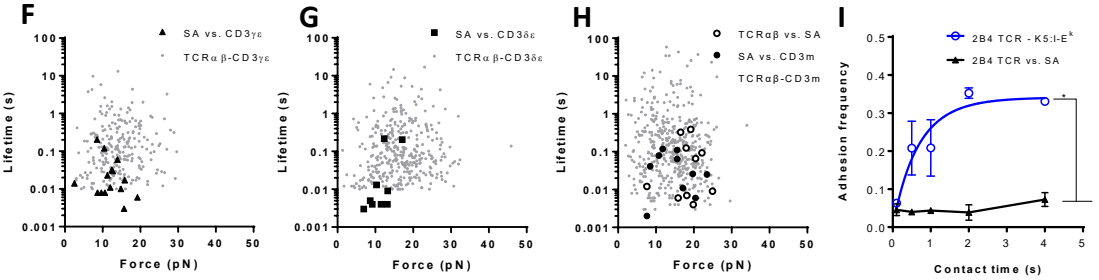

J

Interactions	Effective 2D affinity A_cK_a (10^{-6} μm^4)	Effective 2D on-rate A_cK_{on} (10^{-5} μm^{4}s^{-1})	2D off-rate k_{off} (s^{-1})
TCRαβ-CD3γε	3.8 ± 0.7	5.3 ± 1.0	14.1 ± 0.1
TCRαβ-CD3δε	2.8 ± 0.6	3.1 ± 0.7	11.1 ± 0.5
CD3γε-CD3δε	11.0 ± 4.4	16.4 ± 6.5	14.9 ± 0.4
TCR - K5:I-E^k	2.2 ± 0.9	0.28 ± 0.15	1.3 ± 0.5

Figure S1. Inability for SPR to detect TCR-CD3 3D binding; specificity controls for TCR-CD3 2D binding; kinetics parameters measured by MAF and BFP. Related to Figures 1-3. (A) SIYR:H-2K^b tetramer staining MFI of hybridoma expressing 2C TCR treated with indicated antibodies or antibody fragments. **(B)** 10 μg/mL biotinylated CD3γε and CD3δε were immobilized on streptavidin (SA) sensor chips in a BIACore T200 instrument. 13.1, 26.3, 52.5, 105, or 210 μM TCRαβ were injected over CD3γε (*left*) and CD3δε (*right*) at time = 0 s, and the analyte solution was switched to buffer at 75 s. Analysis of SPR signals by T200 evaluation software 3.0 did not return reliable kinetic parameters. **(C)** Specificity controls for the MAF assay. High adhesion frequencies were observed when both partners of TCRαβ–CD3γε, TCRαβ–CD3δε, and TCRαβ–CD3m interactions were present. Missing either binding partner reduced adhesion frequencies to the background level. **(D)** Effective 2D affinities of homotypic interactions of human CD3γε, CD3δε, and TCRαβ ECDs. **(E)** Specificity controls for the BFP force-clamp and thermal-fluctuation assays. Again, missing either binding partner generated lower adhesion frequencies than those experiments with all binding partners on both sides, which were kept ≤20% to minimize multiple bond events. **(F-H)** The sparse nonspecific bond lifetimes were also generally shorter comparing to those from TCRαβ–CD3γε (*F*), TCRαβ–CD3δε (*G*), and TCRαβ–CD3m (*H*) bond lifetimes. **(I)** Adhesion frequency *vs.* contact duration plot for 2B4 TCR expressing hybridomas interacting with K5:I-E^k coated beads (blue circle). Using SA beads without further pMHC coating to contact the same cells yielded a nonspecific binding curve (black triangle). **(J)** Summary of effective 2D affinities, effective 2D on-rates, and 2D off-rates for TCRαβ–CD3γε, TCRαβ–CD3δε, and CD3δε-CD3γε ECD (purified proteins) interactions, as well as 2B4 TCR (expressed on T hybridoma) interaction with pMHC (K5:I-E^k). Data represent mean ± SD in (*C*) and (*E*), and mean ± SEM in (*D*) and (*I*).

Figure S2

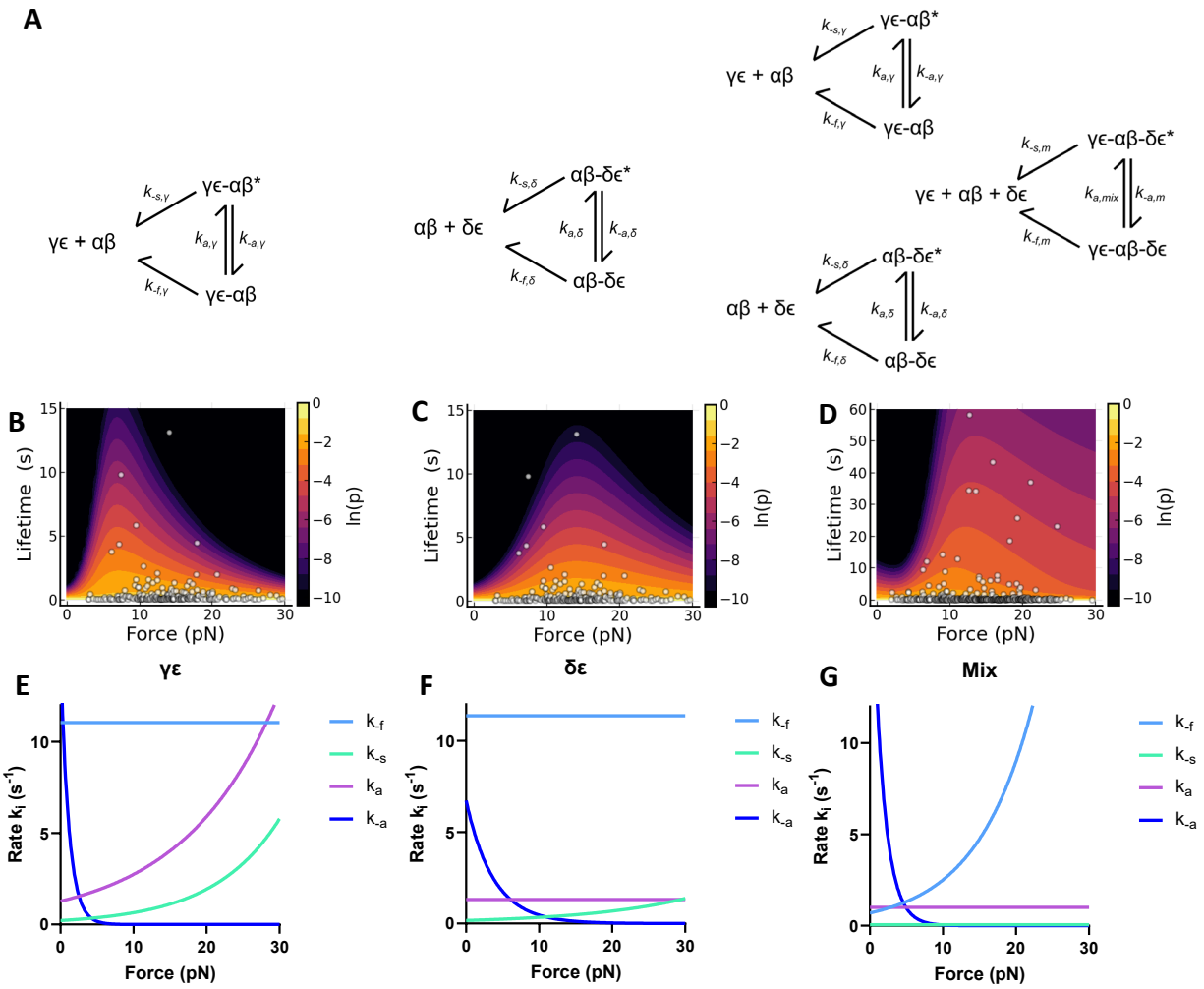

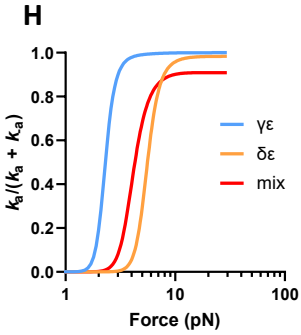

I

Transition	Rate	$k^0_{i,j}$ (1/s)	$x_{i,j}$ (Å)
TCRαβ–CD3γε → 0	$k_{-f,\gamma}$	11.1 ± 0.298	0 ± 0.0685
(TCRαβ–CD3γε)* → 0	$k_{-s,\gamma}$	0.196 ± 0.0228	4.40 ± 0.304
TCRαβ–CD3γε → (TCRαβ–CD3γε)*	$k_{a,\gamma}$	1.60 ± 0.355	1.93 ± 0.801
TCRαβ–CD3γε ← (TCRαβ–CD3γε)*	$k_{-a,\gamma}$	15.0 ± 1.91	- 32.5 ± 2.30
Transition	**Rate**	$k^0_{i,j}$ (1/s)	$x_{i,j}$ (Å)
TCRαβ–CD3δε → 0	$k_{-f,\delta}$	11.4 ± 0.162	0 ± 0.0652
(TCRαβ–CD3δε)* → 0	$k_{-s,\delta}$	0.184 ± 0.0412	2.80 ± 0.422
TCRαβ–CD3δε → (TCRαβ–CD3δε)*	$k_{a,\delta}$	1.50 ± 0.316	0 ± 0.504
TCRαβ–CD3δε ← (TCRαβ–CD3δε)*	$k_{-a,\delta}$	8.77 ± 2.49	- 12.3 ± 1.57
Transition	**Rate**	$k^0_{i,j}$ (1/s)	$x_{i,j}$ (Å)
CD3δε–TCRαβ–CD3γε → 0	$k_{-f,m}$	0.700 ± 0.204	5.45 ± 0.204
(CD3δε–TCRαβ–CD3γε)* → 0	$k_{-s,m}$	0.0519 ± 0.0196	0 ± 0.859
CD3δε–TCRαβ–CD3γε → (CD3δε–TCRαβ–CD3γε)*	$k_{a,m}$	1.00 ± 0.118	0 ± 0.322
CD3δε–TCRαβ–CD3γε ← (CD3δε–TCRαβ–CD3γε)*	$k_{-a,m}$	21.8 ± 9.82	- 26.7 ± 3.21

Figure S2 | Two-state catch bond models fit the force-dependent lifetime data from experiments. Related to Figure 3. (A) Schematics of three two-state catch bond models with indicated reaction rates for TCRαβ–CD3γε (*left*) and TCRαβ–CD3δε (*middle*) bimolecular interactions, as well as for the case of TCRαβ–CD3m interactions where an additional CD3δε–TCRαβ–CD3γε trimolecular interaction is included (*right*). The superscript * labels the strong states. (**B-D)** Bond lifetime *vs.* clamp-force data fitted using maximum likelihood estimation. Depending on the Bell parameters, the three kinetic models generate three families of force-lifetime curves for TCRαβ–CD3γε (*B*), TCRαβ–CD3δε (*C*), and TCRαβ–CD3m (*D*) interactions. The likelihoods for data (points) to be observed as predicted (curves) were maximized to obtain the best-fit parameters (except those directly determined fast dissociation rates from BFP thermal fluctuation assay, shown in Fig. S1J), which are listed in (*I*). Parameters so evaluated from global fitting predict mean ± SD curves of 1) bond lifetime *vs*. force, 2) cooperativity index *vs.* force, and 3) normalized survival probability *vs.* lifetime at 4 force bins that well match the corresponding data in Fig. 3E-G, respectively. **(E-G)** Reaction rates *vs.* force plots. The force-dependent rates for fast and slow dissociations as well as for activation and deactivation state transitions are plotted for the TCRαβ–CD3γε (*E*), TCRαβ–CD3δε (*F*), and TCRαβ–CD3m (*G*) reactions according to Equation 14 and the best-fit Bell parameters. The reciprocal apparent reaction rates in g is the sum of individual reciprocal reaction rates for dimeric and trimeric transitions. **(H)** Fractions of strong state *vs.* force plots for TCRαβ–CD3γε, TCRαβ–CD3δε, and TCRαβ–CD3m interactions. **(I)** Summary of the best-fit Bell parameters used to model the TCRαβ–CD3γε (*top*), TCRαβ–CD3δε (*middle*), CD3δε–TCRαβ–CD3γε (*bottom*) dissociations.

Figure S3

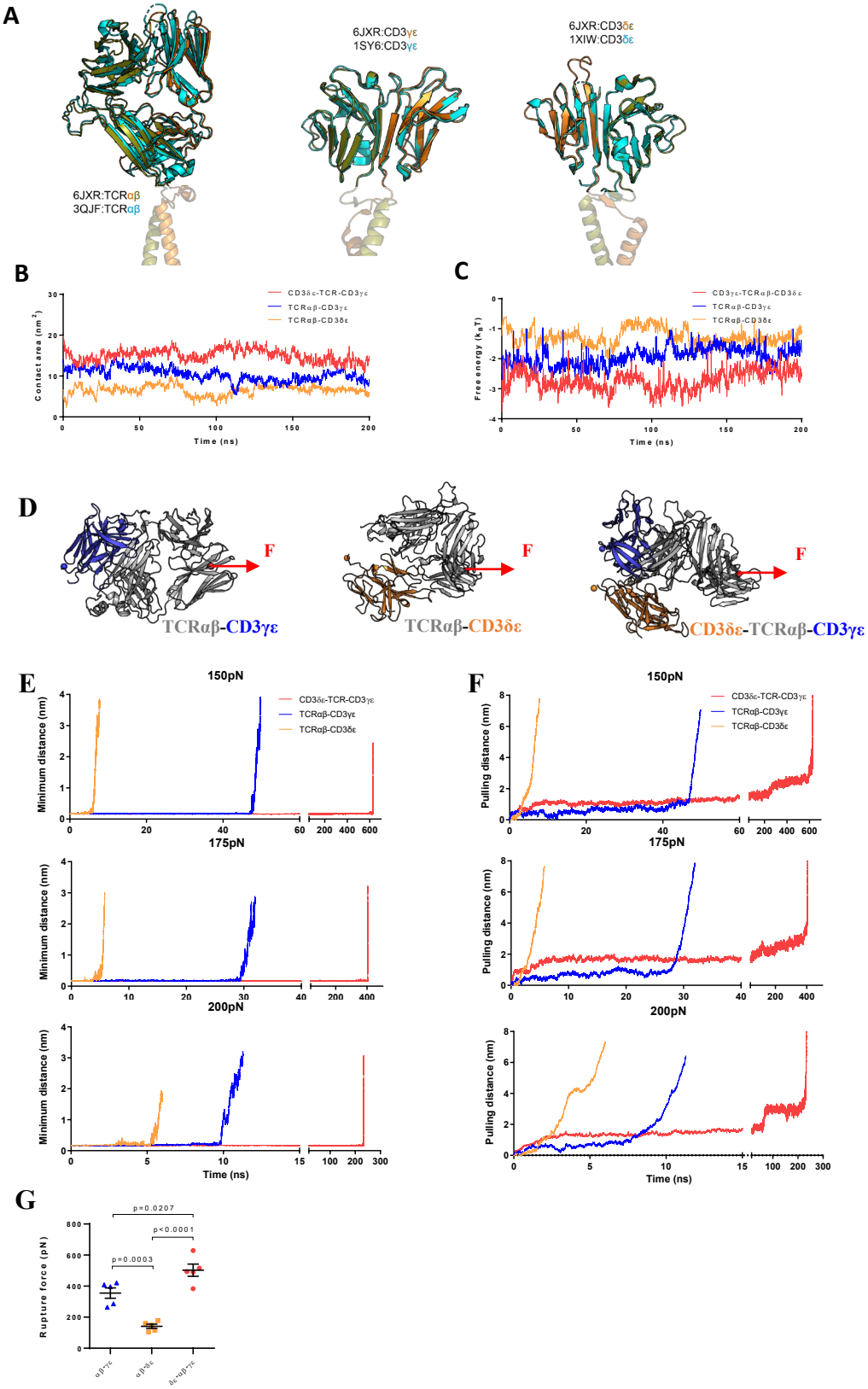
A
6JXR:TCRαβ
3QJF:TCRαβ
6JXR:CD3γε
1SY6:CD3γε
6JXR:CD3δε
1XIW:CD3δε
B
Contact area (nm²)
Time (ns)
CD3δε-TCR-CD3γε
TCRαβ-CD3γε
TCRαβ-CD3δε
C
Free energy (kBT)
Time (ns)
CD3γε-TCRαβ-CD3δε
TCRαβ-CD3γε
TCRαβ-CD3δε
D
F
TCRαβ-CD3γε
TCRαβ-CD3δε
CD3δε-TCRαβ-CD3γε
E
150pN
175pN
200pN
Minimum distance (nm)
Time (ns)
CD3δε-TCR-CD3γε
TCRαβ-CD3γε
TCRαβ-CD3δε
F
Pulling distance (nm)
Time (ns)
G
Rupture force (pN)
p=0.0207
p<0.0001
p=0.0003
αβ-γε
αβ-δε
δε-αβ-γε

Figure S3. Structures used in our studies and MD results. Related to Figure 4. (A) Structural comparisons of the TCRαβ (*left*), CD3γε (*middle*), and CD3δε (*right*) ECDs by superimposing the structures adapted from cryoEM (6JXR) and crystallography (3QJF, 1SY6, and 1CIW, respectively). MD simulations were based on the cryoEM structure, whereas the crystal structures represent the proteins used in experiments. **(B-C)** 200-ns CMD trajectories of contact areas (*B*) and free energy scores (*C*) between TCRαβ and CD3γε (blue), CD3δε (orange), and both (red), analyzed using Gromacs 2019 sasa tool (*B*) and Autodock Vina 1.1.2 (*C*), respectively. **(D)** Initial structures and pulling geometries. Forces were applied to the TCRα N-termini away from the anchored C-termini of CD3γε (*left*), CD3δε (*middle*), and both CD3γε and CD3δε (*right*). **(E-F)** SMD trajectories of minimum distances (E) and pulling distances (*F*) between TCRαβ and CD3γε (blue), CD3δε (orange), and both (red) under 150 (*top*), 175 (*middle*), and 200 (*bottom*) pN. The minimum distance marks the minimal value among all possible pairwise distances between the atoms of the two interacting ECDs. The abrupt increase in the minimum distance indicates dissociation. The pulling distance reports the point-to-point extension between the center-of-mass of the pulling residues and anchor residues in (*D*). The force-extension curves reflect distinctive pulling characteristics (*i.e.*, different interdomain arrangements and elastic responses) in the partially and fully assembled TCR-CD3 complexes. **(G)** Rupture forces at bond dissociation by constant-velocity pulling (force-ramp SMD) on the TCRαβ–CD3γε, TCRαβ–CD3δε and CD3δε–TCRαβ–CD3γε ECD complexes. Ramp forces were applied on the same sites, along the same directions as in (*D*) through a 70pN/nm spring at a velocity of 1 nm/ns to accelerate TCR-CD3 dissociations. Data represent mean ± SEM. p-values were obtained using unpaired Student t-tests.

Figure S4A-C

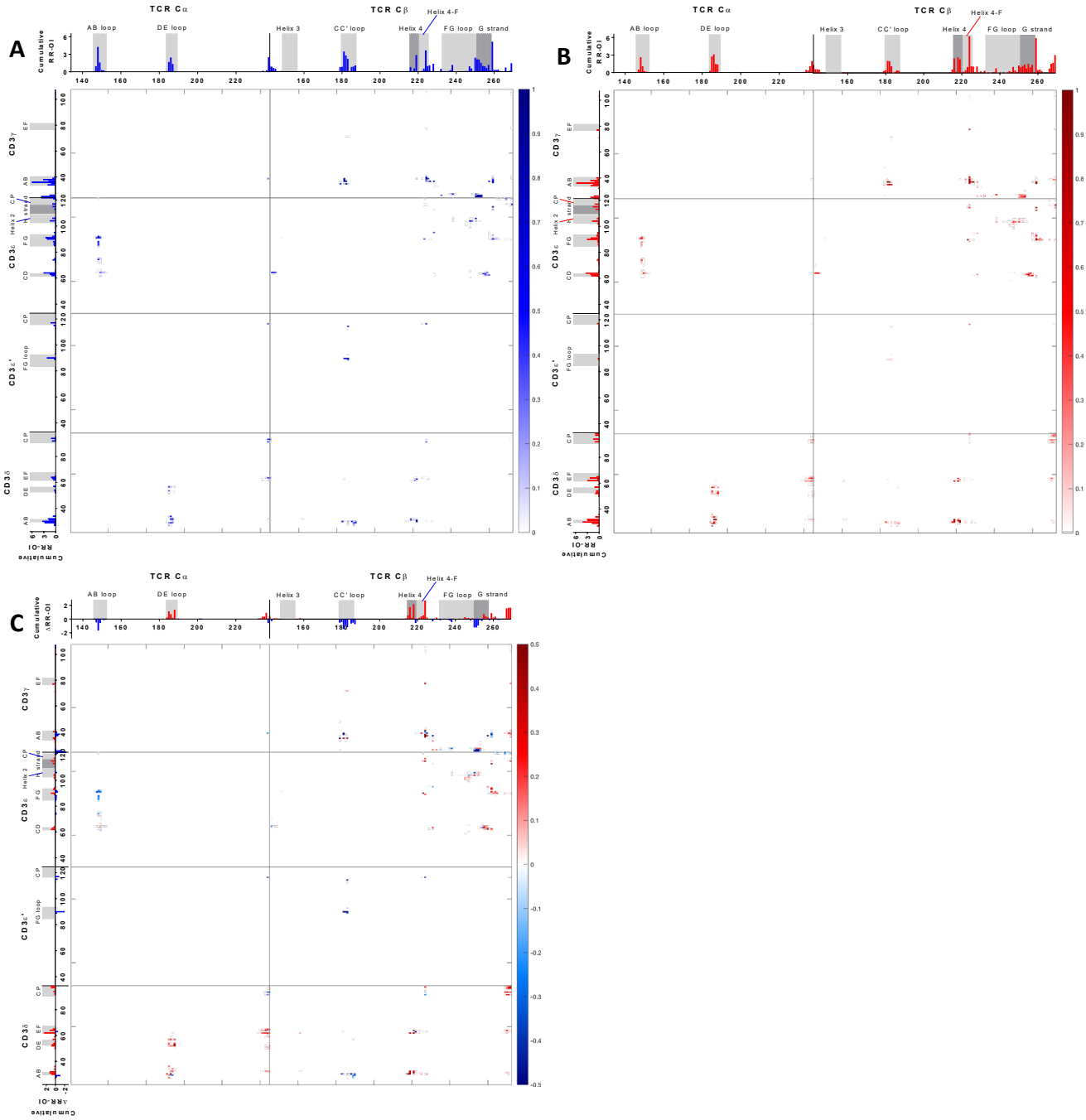
A
B
C
TCR Cα
TCR Cβ
Helix 4-F
AB loop
DE loop
Helix 3
CC' loop
Helix 4
FG loop
G strand
Cumulative RR-OI
Cumulative ΔRR-OI
CD3γ
CD3ε
CD3ε*
CD3δ
Helix 2
A strand

Figure S4D-F

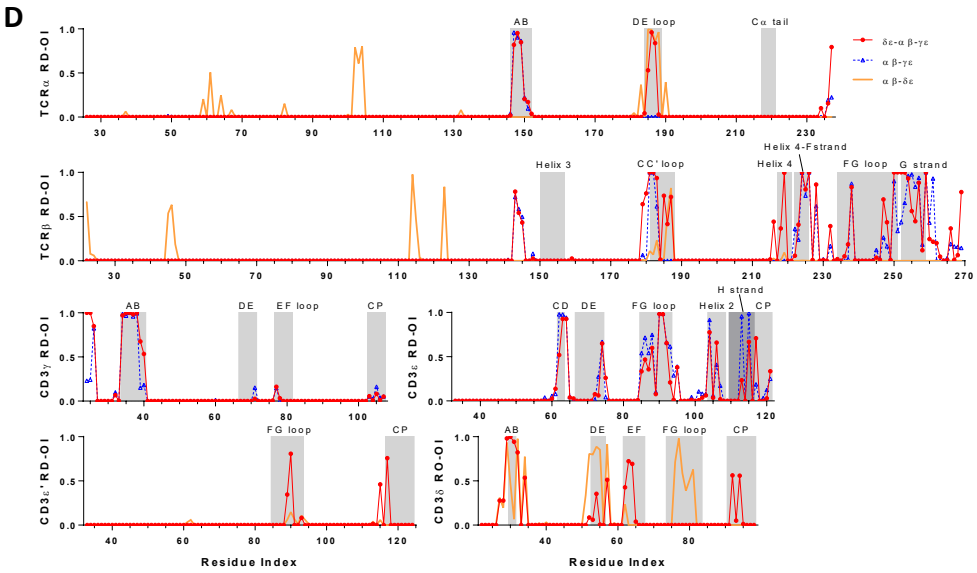
D
TCRα RD-OI
TCRβ RD-OI
CD3γ RD-OI
CD3ε RD-OI
CD3ε' RD-OI
CD3δ RO-OI
AB
DE loop
Cα tail
Helix 3
CC' loop
Helix 4
Helix 4-Fstrand
FG loop
G strand
DE
EF loop
CP
CD
Helix 2
H strand
EF
δε-α β-γε
α β-γε
α β-δε
Residue Index

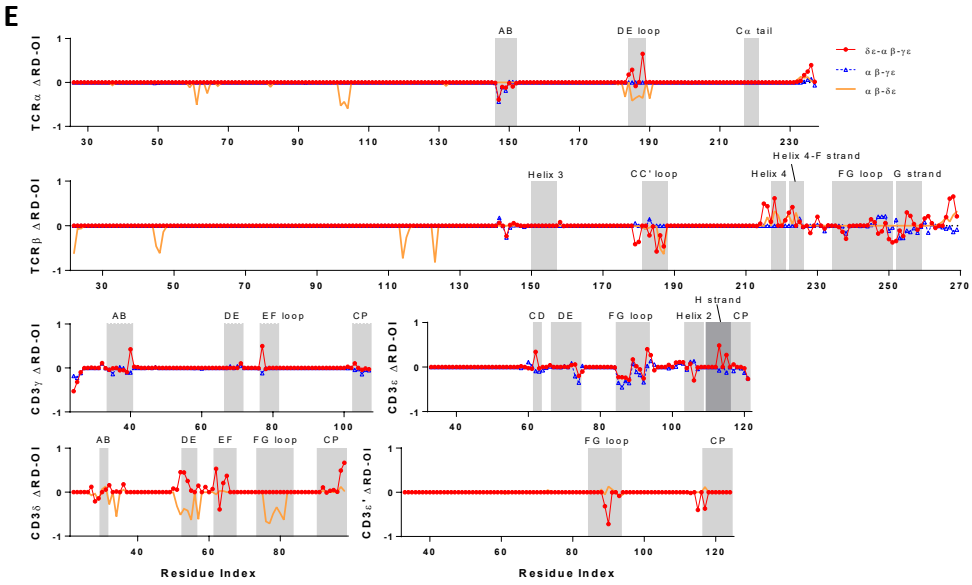
E
TCRα ΔRD-OI
TCRβ ΔRD-OI
CD3γ ΔRD-OI
CD3ε ΔRD-OI
CD3δ ΔRD-OI
CD3ε' ΔRD-OI
AB
DE loop
Cα tail
Helix 3
CC' loop
Helix 4
Helix 4-F strand
FG loop
G strand
DE
EF loop
CP
CD
Helix 2
H strand
EF
δε-α β-γε
α β-γε
α β-δε
Residue Index

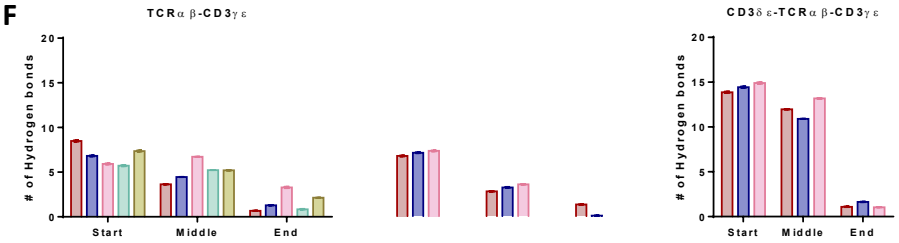
F
TCRα β-CD3γ ε
CD3δ ε-TCRα β-CD3γ ε
# of Hydrogen bonds
Start
Middle
End

Figure S4. RR-OI matrices, RD-OI profiles, and hydrogen bonds at the TCRαβ–CD3 interfaces. Related to Figure 5. (A-C) Matrices display the RR-OI of TCRαβ *vs.* CD3s residue pairs of the CD3δε–TCRαβ–CD3γε trimeric complex. Rows correspond to the TCR residue indices of Cα and Cβ chains from N to C-termini. Columns match the CD3 residue indices aligned from N- to C-termini of CD3δ, ε', ε, and γ chains. The top and left sidebars present the cumulative values over the columns and rows, respectively, indicating the overall contact level of one-to-many interactions for each residue. Three versions of RR-OI matrices are shown: (*A*) Force-free RR-OI, calculated from CMD dynamics; (*B*) Mean force-clamp RR-OI, averaged over individual RR-OI matrices calculated from force-clamp SMD dynamics of 150, 175, and 200 pN; and (*C*) Differential RR-OI, calculated by subtracting (B) from (A). The color coding is such that red indicates force enhancement and blue indicates force suppression of pairwise residue contacts. **(D)** RD-OI profiles of contacting ECDs in TCRαβ–CD3γε, TCRαβ–CD3δε, and CD3δε–TCRαβ–CD3γε complexes from CMD simulations. **(E)** Differential RD-OI profiles of contacting ECDs in TCRαβ–CD3γε, TCRαβ–CD3δε, and CD3δε–TCRαβ–CD3γε complexes, calculated from subtracting d from Fig. 4C. Positive values represent force enhancement, and negative values represent force suppression of the residue contact against its interacting domains. **(F)** The instantaneous hydrogen (H) bond count between TCRαβ and CD3γε (*left*), CD3δε (*middle*), and both (*right*) were tracked throughout SMD simulations. A H-bond was identified by <3.5 Å distance between Donor (*D*) and Acceptor (*A*) atoms and a *D-H-A* angle of 180° ± 30°. H bonds were summarized using the mean of total H-bond numbers in the start (first 1 ns), middle (remaining), and end (last 1 ns) periods under 100, 125, 150, 175, and 200 pN forces for dimeric interactions in (*A*) and (*B*), and 150, 175, and 200 pN forces for trimeric interactions in (*C*). The hydrogen bonds were analyzed using Gromacs 2019 hbond program.

Figure S5

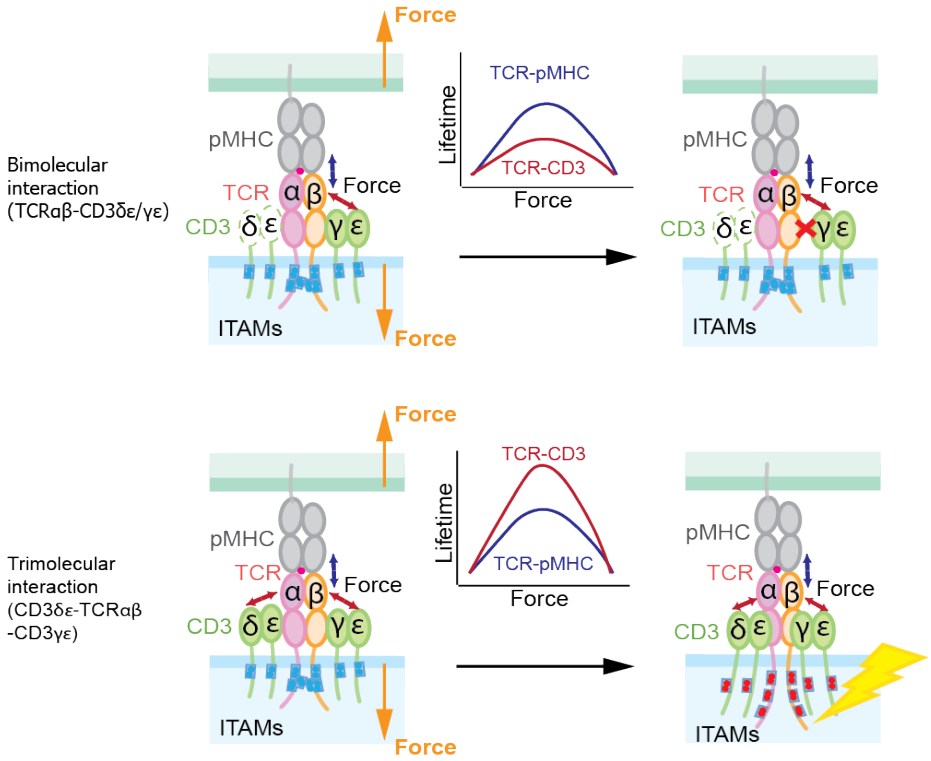

Figure S5. Model of TCR triggering facilitated by force-enhanced TCRαβ–CD3 interaction. Force on TCRαβ via engaged pMHC elicits catch bond formation to prolong its lifetime. The information embedded in the ligand is encoded by force and transmitted from the pMHC through the TCRαβ to CD3s via interactions of the ECDs, CPs, and transmembrane segments to regulate phosphorylation of the ITAMs in the CD3 cytoplasmic domains. *Top*: In the absence of cooperativity, the ECD interactions of TCRαβ with CD3γε and CD3δε are suboptimal and force only elicits two short-lived bimolecular catch bonds that dissociate before the longer-lived TCRαβ–pMHC catch bond, preventing the pMHC from inducing adequate TCR signaling. *Bottom*- The cooperative ECD binding of TCRαβ with CD3γε and CD3δε generates a greatly enhanced catch bond that enables force to prolong the CD3δε–TCRαβ–CD3γε trimolecular bond lifetimes to match those of the TCRαβ–pMHC catch bond, allowing the pMHC to induce appropriate TCR signaling.

Legends for Supplementary Videos and Tables

Supplementary Video 1 | 200 ns CMD simulation of a TCRαβ–CD3γε complex, with the initial TCRαβ (*gray*) and CD3γε (*blue*) configurations modified from the cryoEM structure (6JXR).
Supplementary Video 2 | 200 ns CMD simulation of a TCRαβ–CD3δε complex, with the initial TCRαβ (*gray*) and CD3δε (*orange*) configurations modified from the cryoEM structure (6JXR).
Supplementary Video 3 | 200 ns CMD simulations of a CD3γε-CD3δε complex, with the initial CD3γε (*blue*) and CD3δε (*orange*) configuration modified from the cryoEM structure (6JXR).
Supplementary Video 4 | 200 ns CMD simulation of a CD3δε–TCRαβ–CD3γε complex, with the initial TCRαβ (*gray*), CD3γε (*blue*), and CD3δε (*orange*) configurations modified from the cryoEM structure (6JXR).
Supplementary Video 5 | Force-clamp SMD simulation of TCRαβ–CD3γε dissociation under 175 pN. Forces were applied to TCRαβ (*gray*) at the TCRα N-terminus (*red sphere*) and CD3γε (*blue*) was anchored at the ε-chain C-terminus (*blue sphere*). SMD was initiated from equilibrated structures extracted from CMD, and ended soon after the complex dissociation at ~29.4 ns.
Supplementary Video 6 | Force-clamp SMD simulation of TCRαβ–CD3δε dissociation under 175 pN. Forces were applied to TCRαβ (*gray*) at the TCRα N-terminus (*red sphere*) and CD3δε (*orange*) was anchored at the ε-chain C-terminus (*orange sphere*). SMD was initiated from equilibrated structures extracted from CMD, and ended soon after complex dissociation at ~5.2 ns.
Supplementary Video 7 | Force-clamp SMD simulation of CD3δε–TCRαβ–CD3γε dissociation under 175 pN. Forces were applied to TCRαβ (*gray*) at the TCRα N-terminus (*red sphere*), and CD3γε (*blue*) and CD3δε (*orange*) were anchored at both ε-chain C-termini (*blue* and *orange spheres*). SMD was initiated from equilibrated structures extracted from CMD, and ended soon after complex dissociation at ~403.9 ns.
Supplementary Video 8 | Interface residues between TCRαβ (*gray*) and CD3γε (*blue*). Dynamic RD-OI thresholding (*bottom*) was applied and only contact residues with above threshold RD-OI values were shown from white to red according to dynamic colormap below.
Supplementary Video 9 | Interface residues between TCRαβ (*gray*) and CD3δε (*orange*). Dynamic RD-OI thresholding (*bottom*) was applied and only contact residues with above threshold RD-OI values were shown from white to red according to dynamic colormap below.
Supplementary Video 10 | Interface residues among CD3δε (*orange*), TCRαβ (*gray*), and CD3γε complex (*blue*). Dynamic RD-OI thresholding (*bottom*) was applied and only contact residues with above threshold RD-OI values were shown from white to red according to dynamic colormap below.
Supplementary Video 11 | 3D visualizations of Fig. 5g-i. The full CD3δε'–TCRαβ–CD3γε ECD assembly is shown sequentially by rotating presentations: (1) overview of the trimeric complex (TCRαβ in *gray*, CD3γε in *blue*, and CD3δε' in *orange*). Residues with high RD-OI values combined from both SMD and CMD (sum > 1.5) are highlighted using sticks, colored white to red gradually. (2) ΔRD-OI and (3) ΔRMSF profiles between SMD and CMD are shown by colors (*red* for positive, *blue* for negative and *white* for zero values). The sidechains of the residues with the same high combined RD-OI values as Fig. 5g are highlighted in Fig. 5h. The residues' absolute RMSF values are represented by the thickness of the protein backbone in Fig. 5i.

Supplementary Table 1 | **(Sheet A)** Sum and **(Sheet B)** difference of the two TCRαβ to CD3γε and CD3δε' RR-OI matrices obtained from SMD and CMD simulations respectively, showing all the residues, with subunit names, the residue abbreviations and indices labeled. **(Sheet C)** RD-OI value *vs.* index of TCRα and β residue contacting CD3 ECDs, and of CD3γ, ε, ε' and δ residue contacting TCRαβ ECDs in the TCRαβ–CD3γε, TCRαβ–CD3δε' and CD3δε'–TCRαβ–CD3γε complexes.

Supplementary Table 2 | Sum and difference RR-OI indices between key force-stabilizing and force-destabilizing TCR residues and their interacting CD3 residues.